A review of carbon isotope excursions, redox changes and marine red beds of the Early Triassic with insights from the Qinling Sea, northwest China

Hanxiao Li[a, b], Paul B. Wignall[b], Haishui Jiang[a, c], Muhui Zhang[a, c], Xianlang Wu[a], Xulong Lai[a, c, *]

[a] *School of Earth Science, China University of Geosciences, Wuhan, Hubei 430074, PR China*

[b] *School of Earth and Environment, University of Leeds, Leeds, LS2 9JT, UK*

[c] *State Key Laboratory of Biogeology and Environmental Geology, China University of Geosciences, Wuhan, Hubei 430074, PR China*

Abstract

The Early Triassic was an interval characterized by frequent, large global carbon isotope excursions (CIEs), multiple and widespread anoxic phases, and generally high but fluctuating temperatures. In order to comprehensively understand their inter-relationship, we have investigated the Yiwagou section from the little-known Qinling shelf sea, at the eastern corner of Paleo-Tethys, and evaluated the global marine red bed (MRB) occurrences, redox conditions and CIEs. The anoxic episodes show great variations between different regions, but only during the earliest Griesbachian were they of almost global extent, whilst during other Early Triassic

intervals there is great regional variation of redox trends. Even during the early Griesbachian anoxia was absent in South Tibet and Qinling shelf seas. Smithian MRBs in the latter region are dominated by intraclasts or ooids and are likely to be caused by ferruginous ocean waters advected from the adjacent Paleo-Tethys Ocean. The more widespread Spathian MRBs, mostly developed in the middle Spathian, were also likely a product of advection of anoxic ferruginous waters into shelf areas. Vigorous upwelling at this time is unlikely because this would stimulate high productivity and diagenetic conditions that would have reduced the iron oxyhydroxides responsible for the MRBs. Compilation of 54 $\delta^{13}C_{carb}$ records reveals that the negative excursion in the Smithian, from P2 to N3, ranges in magnitude from -2.9‰ to -9.7‰, the positive excursion from N3 to P3 across the Smithian–Spathian boundary ranges from 2.6‰ to 11.9‰ and its amplitude is greatest in the Northern Yangtze Platform. The similarity of N3 values at Yiwagou with those from the seamount carbonates of the Panthalassa Ocean indicates a good oceanic connectivity at the time of Smithian MRBs formation. The global average of $\delta^{13}C$ values during the P2 and N3 CIEs shows that values are 2.0‰ and 1.1‰ heavier in shallow settings compared to deep settings respectively. In contrast, there is no consistent variation with water depth of the subsequent P3 CIE. Analysis of $\Delta\delta^{13}C_{vert}$ values shows that there are large differences between regions that likely reflects the different stratification histories of epicontinental basins, but there is no global signal at this time. Previous studies have suggested a collapse of the water column carbon isotope gradient during P3 associated with vigorous upwelling, but this pattern is not widespread and is likely a regional signal. The origins of the extreme light carbon isotope values during the mid-Smithian N3 excursion, and the heavy early Spathian P3 excursion, remains unclear and are not easily reconciled with global redox changes. Changes in the proportions of carbonate carbon and organic carbon burial may be important.

1. Introduction

Following the catastrophic environmental changes of the Permian–Triassic mass extinction, the Early Triassic world experienced continuing stresses and perturbations whose origins have been much debated (e.g., Wignall et al., 2016; Goudemand et al., 2019; Song et al., 2019; Lyu et al., 2019). Oceanic redox conditions and seawater temperatures all show high-amplitude changes during this period, along with a varied pattern of originations and extinctions of marine organisms (e.g., Payne et al., 2004; Stanley, 2009; Sun et al., 2012, 2015; Huang et al., 2017). Notable events include an extinction crisis for nekto-pelagic organisms in the late Smithian, coincident with a major positive $\delta^{13}C_{carb}$ shift (Stanley, 2009; Zhang et al., 2019a; Dai et al., 2021; Du et al., 2022). Most ammonoid families became extinct around this time and nearly all Smithian conodont genera also disappeared during the late Smithian–early Spathian, to be replaced by new ammonoid and conodont taxa in the early Spathian (Orchard, 2007; Brayard et al., 2013; Zhang et al., 2019a; Dai et al., 2021).

Ocean temperatures rose rapidly across the Permian–Triassic boundary and remained high throughout the Early Triassic, reaching a peak in middle–late Smithian, before the onset of a gradual cooling trend from the late Smithian (Sun et al., 2012; Joachimski et al., 2012; Chen et al., 2013; Goudemand et al., 2019). Either the thermal maximum or subsequent cooling trend have been proposed as a cause of the nekton-pelagic crisis noted above, although widespread anoxia may also have contributed (e.g., Sun et al., 2012, 2021; Widmann et al., 2020; Song et al., 2021a). Black shales are well known from the middle–late Smithian up to the Smithian–Spathian boundary, but in many regions, there is a rapid transition to marine red beds (MRBs) in the early Spathian (Sun et al., 2015; Song et al., 2017, 2019; Li et al., 2019a). MRBs have been documented from many locations, including South China, Tibet, Japan and California, USA (Galfetti et al., 2008; Brühwiler et al., 2009; Takahashi et al., 2009; Sun et al., 2015; Song et al., 2017; Li et al., 2019a) and have been attributed to a variety of causes including oxidation caused by a cooling climate (Song et al., 2017, 2019; Li et al., 2019a).

Coincident with the marine redox changes and biotic events, the Early Triassic carbon isotope record also shows major changes (e.g., Payne at al., 2004; Song et al., 2013; Zhang et al., 2019a), although the amplitude of the carbon isotope excursions (CIEs) varies considerably from region to region and also with water depth (e.g., Payne et al., 2004; Song et al., 2013, 2019; Lyu et al., 2019; Zhao et al., 2020a; Sun et al., 2021). The origin and significance of these temporal, environmental and spatial variations has been much debated and several alternative and often conflicting models have been proposed. The inter-relationship between these phenomena are far from understood.

In this study, we review and discuss the Early Triassic literature and its debates in the light of a newly examined, highly expanded record of continuous Permian–Triassic deposition in a little studied Paleotethyan region, the Qinling Sea. We provide new facies and palaeontological data in order to investigate the factors responsible for the unusual aspects of the Early Triassic oceans, especially the MRBs. Regional carbon isotope oscillations are compared with an in-depth review of records from other regions in order to investigate and better understand the late Smithian crisis in the context of the tumultuous history of the Early Triassic.

2. Geological setting and stratigraphy

During the late Permian, Laurasia and Gondwana merged to form the supercontinent of Pangea which was embayed by the Tethyan Oceans: Neo-Tethys and Paleo-Tethys (Metcalfe, 2013; Xie and Tang, 2021). The migration of Cimmerian terranes from Gondwana, in the early Permian, to subequatorial paleolatitudes by the middle Permian–Early Triassic, led to the opening of Neo-Tethys and the subduction of the Paleo-Tethys (Muttoni et al., 2009; Metcalfe, 2013; Fig. 1). At the Permian–Triassic transition, the Qinling Sea was a seaway between the South China and North China blocks that opened westwards into Paleo-Tethys (Lai et al., 1992, 1995; Feng et al., 1994; Yin and Peng, 1995; Li et al., 2019b). The Yiwagou and Sai'erlangshan sections provide a record of deposition in a carbonate platform of the Qinling Sea (Lai et al., 1992; Li et al., 2019b, 2022).

The Yiwagou section is located in Têwo County, Gansu Province, northwestern China (Fig. 1). It yields a continuous succession of Upper Permian to Lower Triassic strata and is composed of the Yangu Formation, Zhalishan Formation (565.5 m thick) and Maresongduo Formation (833.8 m thick) (Figs. 2A–2D), which all have conformable contacts (Lai et al., 1994). The nearby Sai'erlangshan section at Zoigê also yields a continuous outcrop of the same three formations (Xiao et al., 1992). The Upper Permian Yangu Formation is mainly composed of grey, thick-bedded limestone, oolitic limestone and dolomite limestone. The Zhalishan Formation is represented by grey or red, thin- to thick-bedded bioclastic and micritic limestones. Red argillaceous limestone is common at Sai'erlangshan in the Zhalishan Formation but this lithology is absent at Yiwagou. The Maresongduo Formation consists of thick-bedded, crystalline dolostone, dolomitic limestone and dolomicrite, which are mostly grey at Sai'erlangshan, but red at Yiwagou. The Yiwagou section has been dated using a combination of conodont biostatigraphy and chemostratigraphy (Li et al., 2022).

3. Materials and methods

A sedimentary log of over 800 m thickness was constructed at Yiwagou, beginning within the Yangu Formation and extending up to the Maresongduo Formation. Samples were collected every couple of metres and a total of 459 thin-section samples were produced. A polarizing microscope (Zeiss Axioscope A1) was used for petrographic analysis and photography. Pyrite framboid analysis was also undertaken on polished sections of limestone or micritic limestone after selection of 28 representative samples. They were coated with platinum and, when present, the size of pyrite framboid populations was measured using a scanning electron microscope (SEM) under backscattered electron (BSE) mode at the State Key Laboratory of Biogeology and Environmental Geology, China University of Geosciences (Wuhan). In addition, micro-Raman imaging was performed on polished sections using a WITec 300 Confocal Raman Imaging system. A 532 nm laser was used and focused by a 50× objective (N.A. = 0.75) for image scans, with a spatial resolution of 0.36 μm per pixel. Laser power was maintained at 8 mW. A 600 g/mm grating was used to cover a wavenumber range of 4000 cm^{-1} with a spectral resolution of 4 cm^{-1}. The data were processed with the WITec Project Five 5.1 Plus software and cosmic rays were removed under 2 cm^{-1} filter. The peak intensity for different mineral bonds was imaged as a colour-coded hyperspectral Raman map for the partly oxidized pyrite grain (ZLS-19), the inner part of a red ooid (sample ZLS-72) and a red intraclast (ZLS-83). The standard Raman spectrum of different minerals in this study are from http://rruff.info/.

To analyze the variability of $\delta^{13}C_{carb}$ values in the Early Triassic, we compiled records from 54 sections (Appendix A) for comparison with the record at Yiwagou (Li et al., 2022). The $\delta^{13}C_{carb}$ negative and positive excursions of this interval have been labelled N1–N4 and P1–P3 by Song et al. (2013), a terminology followed here.

4. Results and Interpretation

4.1. Facies Associations

Based on field features and petrographic analysis, eight microfacies were identified and grouped into four facies associations that correspond to four different environments (Table 1, Figs. 2–4): oolitic shoal, open-marine carbonate platform, storm-dominated inner platform and restricted carbonate platform.

4.1.1. Oolitic shoal

Description: This facies association consists of the single facies type Mf1 which is characterized by light grey, thick beds of oolitic grainstone in the Yangu Formation. Other than ooids which constitute 50–80% of the rock, bioclasts fragments are < 5%, and the remaining component is coarse calcite cement. The ooids (0.5–1 mm in diameter) are well-sorted, mostly rounded, occasionally subrounded, with isopachous fringe cement and well-developed concentric layers consisting of alternating micrite and microspar laminae (Figs. 3A–3B). Locally dolomitization has occurred and a coarse, subhedral dolomite crystals have replaced the original texture (Fig. 3C).

Interpretation: Mf1 is interpreted to represent a high-energy, ooid shoal. Isopachous cements are common in marine-phreatic environments suggesting that the ooids accumulated below the vadose zone, although the partial dolomitization could reflect sabkha-like diagenesis after deposition. However, dolomitized carbonates are notably widespread during the Permian–Triassic transition, an observation attributed to extensive marine anoxia at the time (Li et al., 2021). Oolites are also widespread (primarily in equatorial latitudes) during the Permian–Triassic transition interval, and it has been suggested they show a rapid transition from aragonitic to mixed aragonitic-calcitic (bimineralic) ooids during the crisis, with implications for rapid changes of seawater composition at this time (Li et al., 2015). The Yiwagou ooids recorded here formed during the initial phase of this purported ooid transition and yet they show a bimineralic composition with alternations of recrystallised and dark laminae (Figs. 3A–3B). These occurrences are below the Permian–Triassic transition interval and it is noteworthy that they are also known from the late Early Triassic (Woods, 2013). Thus, bimineralic ooids are a feature of the broad Permian–Triassic interval but are not tightly linked to the time of mass extinction.

4.1.2. Open carbonate platform

Description: Facies association 2 consists of three microfacies Mf2–4 containing bioclastic carbonates (Table 1). In the Yangu Formation, grey, medium to thick bedded brachiopod-gastropod-peloid packstone/grainstone (Mf2) alternates with oolite (Mf1). In the lower and middle parts of the overlying Zhalishan Formation, grey or red, thin to medium bedded bivalve-gastropod packstone (Mf3), alternates with thin to thick bedded wackstone/packstone (Mf4) with the same range of bioclasts as Mf3. Fossils which were originally composed of aragonite are replaced by isomorphous coarse calcite crystals (Figs. 3D, 3G), and the cements in the grainstone or packstone are generally composed of coarse sparry calcite (Figs. 3D–3H). The fossil fragments generally have micritic envelopes (Figs. 3F–3G). Cortoids, with bioclasts at their core, are also common in Mf3 (Figs. 3H).

This association contains diverse shallow marine fossils, including brachiopods, gastropods, bivalves, conodonts, fusulinids, ostracods, foraminifers and calcareous algae in Permian strata and gastropods, thin-shelled bivalves (*Claraia*, *Eumorphotis*, *Entolium*), conodonts, ostracodes, crinoids, and foraminifers (*Glomospira simplex*) above the PTB. Gastropods and bivalves are extremely abundant in the early Induan. Trace fossils are common in this association and include *Thalassinoides*, *Palaeophycus* together with rarer *Chondrites* and *Planolites* (Fig. 2H) (Yang, 1992).

Interpretation: The diversity of benthic fossils and trace fossils in this facies association indicates deposition in a well ventilated, shallow-water carbonate platform environment with the common cortoids suggesting some agitation of the bottom waters. The long-term shift from Mf2 to Mf4 across the PTB marks a gradual increase of the micritic mud content that is likely recording a slow deepening from the Changhsingian to the Griesbachian. This was followed by a prolonged interval of stable water depth with Mf4 dominating until the early Smithian (Fig. 5).

4.1.3. Storm-dominated inner platform

Description: This facies association is dominated by red, pink or grey thin- to thick-bedded calcarenites of Mf5 from the upper part of the Zhalishan Formation. Grains are mainly irregular-shaped, angular intraclasts and bioclasts (mostly foraminifers), occasionally small ooids (micritized but with cortex laminae still visible, 0.1–0.5 mm in diameter). Ooids are cemented by thick, isopachous rim cement (Fig. 4C), some are bimineralic (like those of Mf1) with alternating micritic and micrsopar laminae although most are entirely micrite (Fig. 4B–4D). Occasionally fossils and intraclasts are covered by acicular aragonitic (?) cements, which shows unequal thickness, possibly due to abrasion (Figs. 4E).

Diverse and abundant conodonts (Li et al., 2022), including *Pachycladina*, and foraminifers (*Agathammina austroalpina*, *Ammodiscus incertus*, *A.* sp., *Glomospira sinenses*, *Glomospirella spirillinoides*, *G*. sp., *Turriglomina mesotriasica*), and a few other bioclasts, including bivalves, gastropods and ostracods material occur in Mf5. Hummocky cross laminated strata and horizontal bedding have been observed in the field, they both have thin laminae (1–2 mm), and hummocks are 3–4 cm high (Figs. 2E–2F).

Interpretation: Thick-bedded calcarenite sheets with hummocky cross stratification are a typical product of storm deposition and the dominance of such beds in the later Smithian at Yiwagou indicates considerably storm activity at this time. The calcarenites contain an unusual mix of angular intraclasts or ooids. The former may have been generated by storm-wave loading and fragmentation of a lithified seabed followed. Subsequent transport was probably of only brief duration allowing little time for abrasion. The red colour of these strata is discussed further below.

4.1.4. Restricted carbonate platform

Description: Facies association 4 consists of three microfacies Mf6–8 that dominate Spathian deposition at Yiwagou. The oldest levels occur in the uppermost Zhalishan Formation which consists of grey or light red, thin to thick-bedded ostracod wackestone/packstone (Mf6). The succeeding lower part of the Maresongduo Foramation is mainly light grey (but the weathering surface is sometimes reddish or pink), thick bedded or massive, crystalline dolostone, and thin to thick-bedded dolomicrite, dolomite limestone (Mf7). This facies development dominates in the Maresongduo Formation across the region, being known from the Têwo, Zoigê and Dangchang sections of the South Qinling belt (Lai and Xu, 1992). Dolomite occurs as small, subhedral crystals (0.02–0.05 mm in long axis, Fig. 4J). In the upper part of the Maresongduo Formation, kidney-red, purple-red or grey, medium to thick-bedded peloidal packstone/grainstone beds of Mf8 dominate (Figs. 4K–4L) (Mf8).

Fossils in Mf6 include many ostracods and some conodonts (*Pachycladina qinlingensis*, *Parachirognathus semicircnelus*), at the top of the Zhalishan Formation in Mf7 there are conodonts (*Triassospathodus hungaricus*, *T. qinlingensis*, *T.* sp. indet, *Icriospathodus zaksi*) and gastropods, and in Mf8 there are abundant foraminifers (*Glomospira articulosa*, *Glomospirella vulgaris*) and a few conodonts (*T. clinatus*). Trace fossils of this facies association are *Margaritichnus* and *Lockeia*, with a few *Skolithos*, *Cylindricum* and *Gyrolithes* (Figs. 2G, 2I) (Yang, 1992).

Interpretation: This association is interpreted to have been deposited in a shallow, restricted, low energy nearshore environment (Lai and Xu, 1992). Compared with fossils in association 2, bivalves and gastropods are largely absent whilst ostracods are common. The dominance of this group amongst the peloidal-rich sediment suggests a more restricted environment because ostracods are a eurytopic group, although information on their taxonomic composition would help identify if euryhaline taxa are present. Potentially, the ongoing closure of the Qinling Sea may have restricted marine connectedness (Lai et al., 1992), but see further discussion of this below.

4.2. Pyrite petrography and redox levels

Pyrite framboid population sizes can be used to assess redox conditions with both the mean diameter and size range decreasing with increasing intensity of oxygen restriction (e.g., Wilkin et al., 1996, Wignall et al., 1998). The fossiliferous limestones at Yiwagou are not typical oxygen-restricted facies and it is therefore perhaps not surprising that the analysis of 28 polished sections found 13 samples lacking pyrite, 5 samples with only rare framboids (in Mf4), leaving only 10 samples with common framboids (in Mf4 and Mf6, Fig. 5). These last samples come from beds that bracket the red, storm-dominated inner platform beds in the middle–late Smithian. No pyrite was found in the Griesbachian strata and only one sample from the Dienerian yielded framboids (Fig. 5). Some pyrite framboids were partly oxidized, but their morphology was still clearly preserved allowing their size to be measured.

Mean framboid diameters range from 6.6 to 7.5 µm, with a moderate standard deviation (2.9–3.6 µm), in Mf4 beds from the late Dienerian–early Smithian (Fig. 5). In the Wilkins (mean versus standard deviation) plot these samples are seen to distribute around the anoxic-dysoxic boundary with only two samples from Bed 14 (ZLS-36) and the lower part of Bed 15 (ZLS-51) plotting clearly in the anoxic field

(Fig. 6). These beds are interbedded with MRBs that become increasingly common from this level upwards. Framboids reappear towards the top of the Smithian and range into the basal Spathian (Fig. 5). Size distribution at this level is clearly within the dysoxic field (Fig. 6).

The redox history of the Yiwagou section recorded by pyrite petrography differs substantially from that recorded in the epicontinental basin sections of South China and elsewhere. Marine anoxia is widespread during the middle Smithian to earliest Spathian interval in slope-to-basin sections in South China (e.g., Sun et al., 2015; Lyu et al., 2019; Song et al., 2019), South Tibet (Li et al., 2019a), the Sverdrup Basin of the Canadian Arctic (Grasby et al., 2012), clastic ramps in Spitsbergen, Norway (Wignall et al., 2016) and the Neotethyan continental margin of Arabia (Clarkson et al., 2016). Only the younger interval of dysoxic conditions at Yiwagou, in the latest Smithian, overlaps in age with this widespread Smithian–Spathian anoxia interval (Fig. 7).

4.3. Marine Red Beds

Red-coloured strata are developed at many levels in the Yiwagou section: thin beds occur in the earliest Griesbachian and continue to be scattered throughout the late Griesbachian–middle Smithian succession. Red beds then dominate the mid-late Smithian strata and thick red bed units occur in the mid-Spathian (Fig. 7). Raman images of oolites and bioclastic packstones from the red-coloured Smithian strata show that the red pigmentation is due to micron to nanometre-size iron oxides grains of which goethite is the main component although hematite is also present (Fig. 8).

Thin section analysis of the red, oolitic grainstones shows the red pigmentation occurs within ooids and the angular intraclasts (Figs. 4B–4G), and sometimes within micritic matrix but it is not found in the cement.

Authigenic iron oxides in MRBs are generally observed to consist of nanometer -scale particles that contrast with iron oxides derived from terrigenous input which are larger, angular particles (Cai et al., 2012; Hu et al., 2012; Gledhill and Buck, 2012; Song et al., 2017, Li et al., 2019a). Based on this observation, we consider most of the iron oxide content of the Yiwagou ooids and intraclasts to be authigenic (Figs. 4A–4C, 4E–4G), with only few grains in the matrix of possible detrital origin (Fig. 4F). Matheson et al. (2022) have documented iron ooids, composed entirely of hematite, with subsidiary apatite and chamosite, and interpreted them to have grown diagenetically, immediately below the sediment surface as a type of small concretion. However, in the case of the ooids documented here, the majority of the cortices are carbonate with only a few iron oxide laminae, and we interpret them to have grown primarily on the seafloor in agitated conditions like traditional ooids. Brief periods of burial in the sediment may have allowed the formation of goethite laminae by precipitation from iron (ferrous)-rich porewaters or such laminae may have grown on the seabed whilst the ooids were bathed in ferrous-rich bottom waters. The source of such waters is discussed below.

5. Discussion

5.1. Early Triassic anoxic events and marine red beds

The Permian–Triassic mass extinction has long been linked with the development of widespread marine anoxia (e.g., Wignall and Twitchett, 2002; Clarkson et al., 2016; Grasby et al., 2021), with such conditions persisting throughout the Early Triassic and inhibiting rapid recovery (e.g., Hallam, 1992; Sun et al., 2015; Huang et al., 2017). It is therefore interesting that the Yiwagou section records well oxygenated deposition throughout much of this interval including the Permian–Triassic boundary level. The Qinling Sea location is also unusual in showing a surprisingly long-ranging *Hindeodus* fauna which persists from the PTB to around the end Dienerian (Li et al., 2022). However, there may be a hiatus at the extinction level (cf., Li et al., 2022), and it is possible that a short, albeit brief, phase of oxygen-poor conditions is unrecorded at Yiwagou. The common occurrence of MRBs in the Qinling shelf seas offer some clue to the unusual state of ocean redox in this region at this time, as we explore further below.

A compilation of Early Triassic oceanic redox fluctuations shows substantial regional and temporal variations (Fig. 7). Our meta-analysis is based on studies that have used a combination of sedimentological and geochemical indices and confirms the widespread nature of the oxygen-poor/anoxic deposition. Only in the basal Griesbachian were these conditions almost global, with the exception that an anoxic episode is not known from the Qinling Shelf Sea (Fig. 7B) or South Tibet (Fig. 7F) during this time. However, there is a short hiatus at the Yiwagou section in the former region and around the PTB in the latter region (Wignall and Newton, 2003) , raising the possibility that an anoxic episode in these regions is unrecorded. The only other signal to emerge from the analysis is the observation that anoxic facies are less widespread in the late Dienerian/early Smithian, notably disappearing from Boreal shelf seas (Fig. 7).

The variable development of Early Triassic ocean anoxia could be attributed to a variety of causes. It may reflect a true regional variability or it may reflect difficulties of precisely dating and correlating sections from widespread regions, the differing resolution of the individual studies and the different depositional settings of the study sites. Highest resolution studies show that the anoxic interval can be resolved into multiple anoxic events (e.g., Zhang et al., 2020a). Redox conditions also varied between oceans. In particular, the Neo-Tethyan record from the Arabian margin (Clarkson et al., 2016) and South Tibet (Wignall and Newton, 2003) differ substantially from that seen in other regions, notably in their well-ventilated record during the Griesbachian in the immediate aftermath of the mass extinction (Fig. 7). The Qinling shelf sections were also comparably well ventilated at this time. The Panthalassa Ocean was intensely anoxic/euxinic around the PTB but such conditions persisted into the later Early Triassic in equatorial regions sampled in Japanese sections (Fig. 7).

Whilst detailed regional redox variations can come from proxies such as trace metal enrichments and iron speciation, the geochemical proxies $\delta^{238}U$ fluctuations provide a broad overview of the global extent of marine anoxia that gives an independent record of Early Triassic redox (e.g., Cui et al., 2021; Zhang et al., 2018, 2019b). Modelling of the $\delta^{238}U$ changes indicates that seafloor anoxia was extensive around the PTB (Zhang et al., 2020; Cui et al., 2021) and even more so during the mid-late Smithian (Zhang et al., 2019b; Zhao et al., 2020a), confirming some aspects of the regional compilations. Thus, the improvement in oxygenation in the late Dienerian–early Smithian seen in many regions is also manifest in the global proxy records (Fig. 7). However, the increased area of anoxic seafloor in the earliest Spathian, suggested by $\delta^{238}U$ records, is not reflected in the regional records.

MRBs are also common in the Early Triassic, especially in the mid Spathian (Fig. 7), and their occurrences have also been linked with ocean anoxia (Sun et al., 2015; Song et al., 2017; Li et al., 2019a). However, comparing the global records of MRBs and anoxia of the Yiwagou succession shows little in common with other regions except for the presence of red beds in the early-mid Spathian which are widespread in Tethyan regions and also seen in deep-ocean records of Panthalassa (Fig. 7). Two distinct oceanographic models have been proposed for these Spathian MRB occurrences. In South China, MRBs have been ascribed to the reoxygenation of ferruginous ocean waters and precipitation of iron oxides following a prolonged mid Smithian–early Spathian episode of ocean anoxia (Sun et al., 2015). A different situation pertained on the Perigondwanan margin, where Spathian MRBs developed up-dip of a contemporaneous anoxic basin in outer platform settings (Li et al 2019a). In this region the ferruginous waters are therefore said to have upwelled onto the shelf. However, it is unlikely that such upwelling will have supplied nutrients and elevated primary productivity because the increased organic matter flux would have consumed the highly reactive iron oxide nanoparticles forming in the sediment. Thus, the ferruginous waters would need to have been advected onto the shelf without recourse to vigorous upwelling (Matheson et al., 2022). The Li et al. (2019a) model therefore requires there to be a subtle balance between supply of significant ferrous iron but not nutrients. This may have been achieved by the sequestering of phosphorus by the flux of iron oxide nanoparticles into the sediment.

So, what model can be invoked for MRBs at Yiwagou? Here the thickest and most persistent development is in the Smithian strata where they are associated with high-energy storm facies. More minor red beds are also developed in the relatively proximal Sai'erlangshan section (Zhu et al., 2012). At Yiwagou the MRBs are bracketed by strata with abundant framboids indicating dysoxic (and briefly anoxic) conditions. Productivity may have been somewhat higher both before and after the MRB development leading to the development of organic matter remineralization within the sediments and framboid (rather than iron oxide nanoparticle) formation (Fig. 9C). During the prolonged interval of red bed formation ferruginous waters, advecting from the adjacent anoxic Paleo-Tethys Ocean, may have supplied the levels of iron (but not nutrients) required for red bed formation (Fig. 9B). It is unclear if the ocean waters of the adjacent Paleo-Tethys Ocean were anoxic during the Smithian because, of all the oceanic realms at this time, this one is the least known (Fig. 7). Based on global redox proxies, the Smithian MRBs of the Qinling shelf sea coincide with a globally intense/extensive phase of anoxia (Fig. 7). Therefore, the model of Li et al. (2019a) may be appropriate in which ferruginous waters were advected (but not vigorously upwelled) from the adjacent ocean (Figs. 9A–9B).

The situation for the Spathian MRBs at Yiwagou is somewhat different because the fauna suggests a more restricted setting (see above) and the interval was marked by a decline in the extent of ocean anoxia (Fig. 7). In this case the scenario of Sun et al. (2015) may be appropriate: advection of ferruginous waters, flushed from a re-oxygenating ocean, in a very low productivity seaway could have produced iron oxide precipitation in the surficial sediments (Fig. 9). The implication for such a model is that the Qinling shelf was reasonably well connected to the ocean waters in the Spathian despite its restricted fauna. These two apparently contradictory features could be due to different reasons: global ocean circulation enhanced during cooling across SSB supplied ferruginous waters (Song et al., 2019), whilst the losses during the Smithian–Spathian crisis resulting in an impoverished rather than restricted assemblages in the Spathian.

Potentially, the iron source in the Qinling Sea could come from abundant terrestrial runoff rather than oceanic advections. Matheson et al. (2022) refer to this as the "traditional model" of red bed formation and it has been widely proposed for many Phanerozoic MRBs. For the Qinling Sea MRBs this model is supported by their preferential occurrence in the nearshore Sai'erlangshan location, close to the Songpan-Ganzi hinterland and thus a potential source of terrestrial iron (Fig. 1) (Lai et al., 1992). However, our Raman spectral analysis did not find any detrital iron oxide grains and the Lower Triassic succession consists entirely of carbonates indicating there was little/no runoff into the Qinling Sea. Therefore, advection of ferruginous deeper waters into a generally low productivity, carbonate sea is more likely to be the dominant process for the MRB formation in the Qinling shelf seas of the Early Triassic.

5.2. Carbon isotope fluctuations and Early Triassic ocean anoxia

The substantial carbon isotope excursions of the Early Triassic also provide clues to the evolving redox state of the oceans and may help in determining environmental conditions during MRB formation. The Permian–Triassic boundary is marked by a major negative CIE (N1) in many locations but this is only weakly developed at Yiwagou (Fig. 10), possibly because it is mostly unrecorded at a boundary hiatus (Li et al., 2022). The subsequent excursions of the Early Triassic include two large, positive CIEs in the earliest Smithian and Spathian, separated by a major negative perturbation in the middle–late Smithian, labelled P2, N3 and P3 respectively (Song et al., 2013; Sun et al., 2021). These CIEs are clearly manifest in the Yiwagou section (Fig. 10). The amplitudes of these C isotope shifts, particularly that from N3 to P3, are amongst the largest of the Phanerozoic and they imply major changes in carbon cycling (e.g., Du et al., 2022). The gradient between shallow and deep carbon isotope values ($\Delta\delta^{13}C_{vert}$) has also been used to evaluate environmental factors such as the degree of water column stratification (Song et al., 2013).

Several models have been proposed to explain the changing $\delta^{13}C_{carb}$, $\Delta\delta^{13}C_{vert}$, and marine redox records of the Early Triassic including a major emission of volcanic CO_2 from the Siberian Traps as a cause of both the N1 and N3 CIEs (Payne et al., 2004; Payne and Kump, 2007; Galfetti et al., 2007; Song et al., 2019; Shen et al., 2019; Du et al., 2022). There is indirect support for this proposition using mercury concentrations in marine sediments as a proxy for the intensity of volcanism (Shen et al., 2019). However, the mercury spike during N3 is not of the same magnitude to that seen during N1 (Grasby et al., 2016) and yet the N3 CIE is of similar or substantially greater magnitude to the N1 CIE (Song et al., 2013). Evidence for substantial volcanism during the mid-Smithian is also missing from the Siberian region (Hammer et al., 2019; Widmann et al., 2020). It thus appears that the very light $\delta^{13}C_{carb}$ values of N3 cannot be unequivocally attributed to volcanism. Alternatively, N3 has been linked with the purportedly extensive oceanic anoxia of the interval (Zhang et al., 2021). Horacek et al. (2007) suggested overturning of a stratified ocean would upwell deep ^{12}C-rich enriched waters producing light $\delta^{13}C_{carb}$ values into shallow waters. In a distinct but similar model, Zhang et al. (2021) suggested that transgression and upward expansion of stratified waters would introduce the deep ^{12}C-rich waters into shelf areas. Redox implications differ between these alternatives: the vigorous overturn of the Horacek model implies improved oxygenation during N3 whilst Zhang and colleagues suggest the spread of anoxia. The former model is not supported by the global redox record, because widespread re-oxygenation is not observed during N3 (Fig. 7). In contrast, Zhang et al. (2021) note that the uranium isotope record broadly suggests increased spread of anoxia during N3 (Zhang et al., 2019b), although the details of the curve do not closely parallel the $\delta^{13}C_{carb}$ trends (Zhao et al., 2020a). In indirect support of the Zhang et al. (2021) model, the earlier N1 CIE at the start of the Triassic also coincides with a major transgression and spread of anoxia in shelf seas.

The origin of the N3 CIE remains controversial and the same can also be said for the subsequent major increase in C isotope values that lead to the P3 CIE. An increase in $\delta^{13}C_{carb}$ can be driven by substantial burial of light organic matter and this process has been regularly invoked to explain the shift from N3 to P3 (e.g., Payne and Kump, 2007; Widmann et al., 2020; Du et al., 2022) and also the earlier P2 CIE (Stebbins et al., 2018). Given that organic C burial is typically associated with anoxic deposition, it is therefore surprising that the N3 – P3 trend coincides with a rapid decline in oceanic anoxia according to the U isotope proxy (Zhao et al., 2020a), and many sedimentary records show a loss of black shales in the earliest Spathian (e.g. Sun et al., 2021). The extent of anoxia during the Smithian–Spathian transition calculated from $\delta^{238}U$ records varies considerably (Fig. 7), because the absolute values in the studies of Zhao et al. (2020a) and Zhang et al. (2019b) differ slightly and there is also uncertainty when applying a diagenetic correction factor. Nonetheless, both studies clearly show a rapid decline in the extent of anoxia coincident with the P3 CIE.

A purported trend of increasing $\delta^{34}S_{CAS}$ has been offered as evidence for increasing pyrite burial in the N3 – P3 interval (Stebbins et al. 2018), but the supporting data are not nearly as clear-cut as the earlier positive S isotope perturbation seen during P2 CIE. Furthermore, other $\delta^{34}S_{CAS}$ records show a steep increase in values at the start of the Spathian that persist long after the P3 CIE (Du et al., 2022). The lack of support for increased productivity during P3 is side-stepped in many models by suggesting that the enhance burial of organic C was focused in high-productivity upwelling zones of limited extent (Galfetti et al., 2007; Payne and Kump, 2007; Lyu et al., 2019; Song et al., 2019), but the issue remains that such areas have not been identified and their existence is not supported by the U isotope record. In addition, physical evidence for high productivity during the Smithian–Spathian transition, such as phosphorite deposition, is lacking (Sun et al., 2021). Potential, indirect evidence for this mixing comes from the collapse of the $\Delta\delta^{13}C_{vert}$ gradient between N3 and P3 (Song et al., 2013). During N3 surface water $\delta^{13}C_{carb}$ is reportedly up to 10‰ heavier than values from basinal waters, suggesting a water column gradient that is over three times steeper than seen in modern oceans (Song et al., 2013). In contrast, the gradient declines during the transition to P3 and in some locations disappears altogether suggesting a break down in ocean stratification that is perhaps supportive of increased upwelling at this time.

We have re-examined the magnitudes and regional variability of $\delta^{13}C$ and $\Delta\delta^{13}C_{vert}$ records between the P2 to P3 CIEs (late Dienerian–early Spathian) based on a large literature compilation (Figs. 11, 12, Appendix A). This reveals that the magnitude of P2, N3 and P3 varies considerably. The P2-N3 negative excursion ranges from -2.9‰ to -9.7‰, whilst the N3-P3 positive excursion ranges from 2.6‰ to 11.9‰ with the amplitude being greatest in the Northern Yangtze Platform (Fig. 12). In detail, the N3 values show their largest ranges in the North Yangtze Platform and Panthalassa Ocean. In South China, the P3 values in the North Yangtze Platform are all higher than those in the Nanpanjiang Basin. The data from Yiwagou are the only record available from the Qinling Sea and this shows that the $\delta^{13}C_{carb}$ values are consistently amongst the heaviest values known for the P2, N3 and P3 CIEs (Fig. 12).

As previously observed, the CIE values also show variation with water depth: P2 and N3 on average have heavier isotopic values in shallow waters than in intermediate and deep waters whilst P3 CIE values show no consistent variation with water depth (Fig. 11). Compilation of data from 54 sections worldwide (Appendix A), shows that the global average $\delta^{13}C$ values of P2 and N3 CIEs are 2.0‰ and 1.1‰ heavier in shallow settings than deep settings respectively (Fig. 11). And the distribution analyses show that these data commonly follow a normal distribution, with a few exceptions (Appendices B, C). The P3 values show the greatest range in shallow settings but show no consistent variation with water depth (Fig. 11). Because the $\Delta\delta^{13}C_{vert}$ values should be estimated within one single basin or region (e.g., Song et al., 2013, Meyer et al., 2011), three distinct regions have therefore been chosen to evaluate this value: the Nanpanjiang Basin, the Lower Yangtze Basin, and the Arabian Margin, the former two are in Eastern Tethys and the last one is in Neo-Tethys (Figs. 1, 12). In the Nanpanjiang Basin, the $\Delta\delta^{13}C_{vert}$ value during P2 is up to ~5.5‰, but decreases to ~2.8‰ during N3, and then reverses to ~-2.6‰ during P3. However, the lightest $\delta^{13}C$ value of P3 from the deep-water Lekang section of the Nanpanjiang Basin is questionable, and requires further study (Tong et al., 2007). In the Lower Yangtze Basin, six sections provide a shallow-to-deep gradient of carbon isotope values: the shallow-water Yashan section, the moderate water depths of the Meishan section and the deep-water Hushan, West Pingdingshan, North Pingdingshan and South Majiashan sections (Appendix A). During P2 $\Delta\delta^{13}C_{vert}$ values are ~4.9‰, N3 values are ~4.8‰, and P3 remains positive at ~4.4‰ (Fig. 12). In the Arabian Margin, $\Delta\delta^{13}C_{vert}$ values for P2 is ~-3.2‰, N3 is ~2.2‰, P3 is ~-5.4‰. By examining these three separate regions it can be seen the $\Delta\delta^{13}C_{vert}$ values in different regions show major differences. Thus, the collapse of the carbon isotope gradient during P3, as first observed by Song et al. (2013) in South China, is not seen in the Lower Yangtze Basin, whilst the gradient reverse during both P2 and P3 in the Arabian Margin records (Fig. 12). The shallow-water Yiwagou section is close to the Lower Yangtze Basin in the Early Triassic (Fig. 1), and it also follows the same pattern (red stars in Fig. 12). It is important to note that the carbon isotope values are obtained from limestone within epicontinental basin and shelf sea settings and so they need not necessarily reflect the gradient seen in the adjacent open ocean settings as often inferred. The $\Delta\delta^{13}C_{vert}$ gradients within such basins may only record regional stratification intensity. We suggest that the $\Delta\delta^{13}C_{vert}$ data suggest stratification was widespread (and of variable intensity) in Early Triassic basins and gradually declined from the Smithian onwards except in the Lower Yangtze Basin.

The value of $\delta^{13}C_{carb}$ is dependent on several factors including water column productivity, carbonate composition and (especially important in carbonate platform settings) connectivity with the world's oceans. The modern Bahamas Bank has lighter values than adjacent oceanic waters due to remineralization of marine and terrestrial organic matter in platform settings (Patterson and Walter, 1994). Thus, transgression and deepening of a carbonate platform can enhance circulation in platform-top waters and lead to more positive values of $\delta^{13}C$ as they tend toward oceanic values (Immenhauser et al., 2003). In this scenario the $\Delta\delta^{13}C_{vert}$ is at least partially controlled by sea-level change and water mass connectivity. This notion helps explain the generally heavier $\delta^{13}C$ seen at Yiwagou compared to the more restricted regions such as the North Yangtze Platform (Fig. 11). Yiwagou was located in a carbonate platform on a continental margin facing the Paleo-Tethys Ocean with its presumed heavier $\delta^{13}C$ surface water values. In comparison, the North Yangtze Platform was located within the extensive epicontinental seas of this continent and would be expected to have lighter values as is observed. Also, the generally greater variability of North Yangtze Platform values could reflect the rather variable degree of connectivity of the region. In contrast, during the N3 excursion the Yiwagou, carbon isotope values overlap with those from the seamount carbonates of the Panthalassa Ocean (Fig. 11). This suggests good oceanic connectivity at the time of Smithian MRB formation in the Qinling Sea and supports the idea that advection of ferruginous ocean waters was possible at this time. On the flip-side of the coin, the general lack of MRBs in the Smithian (Fig. 7), other than the Qinling occurrences, suggests connections between epicontinental seas and oceans was generally poor at this time. This implies that the widespread mid-late Spathian MRBs formed at a time of greater connectivity.

So, where does this leave the unusual reversal of vertical $\delta^{13}C_{carb}$ gradients during the Smithian–Spathian transition? This reversal is widespread, of variable magnitude and is not a global pattern. As noted, a re-invigoration of global-ocean circulation could be linked to contemporaneous global climatic cooling (Sun et al., 2012; Romano et al., 2013) and stimulated marine productivity through enhanced upwelling of nutrients is a highly popular model (e.g., Song et al., 2013; Zhang et al., 2015; Stebbins et al., 2018; Lyu et al., 2019; Zhao et al., 2020a; Du et al., 2022), but not one receiving much support from geochemical and sedimentological records (Zhang et al., 2019b; Zhao et al., 2020a; Sun et al., 2021). Whilst the $\Delta\delta^{13}C_{vert}$ transition could reflect a loss of stratification within many epicontinental basins, invigorated oceanic upwelling need not be a corollary.

The ultimate cause of the two principal positive excursions of the Early Triassic (P2 and P3) also remains enigmatic. Neither episode coincides with clear evidence for enhanced oceanic anoxia (Fig. 7), which ensures that scenarios invoking enhanced organic C burial remain moot. A similar issue occurs with the Kamura Event: a Middle Permian interval with heavy positive $\delta^{13}C_{carb}$ values (+5‰) that also does not coincide with globally elevated organic C deposition (Bond et al., 2010; Zhang et al., 2020b). Potentially, this positive CIE can be modelled as a proportional increase of organic C burial relative to carbonate burial as suggested for the Kamura Event (Zhang et al., 2020b). Unfortunately, this scenario does not translate easily to the Spathian CIE because a positive Ca isotope trends suggests that there was a massive increase of carbonate burial at this time (Zhao et al., 2020b). However, this trend is not replicated in the data of Song et al. (2021b) which instead suggests that there was a carbonate crisis around the Smithian–Spathian transition (cf. Galfetti et al. 2007). More studies are clearly needed of these various isotope systems but it is possible that the major CIEs of the Early Triassic are controlled by both fluctuations of organic carbon burial and changes in the proportion of carbonate versus organic carbon deposition. Biogeochemical box modelling could help to distinguish between these factors controlling CIEs (e.g. Zhang et al 2020b), especially during the enigmatic Smithian–Spathian transition. Further investigation is also merited of the relationship between regional sea-level fluctuations and CIEs because the role ocean connectivity (e.g. the Immenhauser et al. (2003) model) has rarely been explored in studies of the Early Triassic.

6. Conclusions

The Qinling Sea region (Yiwagou and Sai'erlangshan sections) records a distinct shallow-water history of deposition during the Permian–Triassic boundary interval. In the Early Triassic that features a much better oxygenated depositional history than seen in many other contemporaneous shelf sea regions. Four different environment settings are recognized: oolitic shoals in the Changhsingian, an open-marine carbonate platform from late Changhsingian to middle Smithian, a storm-dominated inner platform in the middle–late Smithian and restricted carbonate platform from latest Smithian to Spathian. A diverse marine community occurs in the Griesbachian–Smithian interval but in the Spathian an ostracod-dominated fauna suggests restricted marine conditions at this time.

The Qinling Sea also witnessed the prolonged deposition of marine red beds, which dominate Smithian and younger Spathian strata. A review of MRB occurrences globally finds that they are common in the latter of these two intervals, whilst Smithian examples have not previously been recorded. The traditional model for red bed formation – enhanced input of terrigenous iron – is not appropriate for the Qinling Sea MRBs which were deposited in a carbonate-dominated setting receiving little clastic input. An advection model is proposed to explain red bed formation with ferruginous waters, flushed from adjacent Paleo-Tethys ocean waters. Productivity within the Qinling seas is likely to have been very low in order to have facilitated the preservation of the highly reactive iron oxide nanoparticles that impart the red colour to sediments. Pyrite petrography study at Yiwagou shows the presence of abundant framboids in strata straddling the Smithian MRBs. This suggests the development of dysoxic conditions in presumably more productive waters in the early Smithian and earliest Spathian.

Compilation of global redox history and MRBs shows multiple anoxic periods from Griesbachian to Spathian with notable regional variations, especially in the Qinling Shelf Sea. Only during the PTB and basal Griesbachian are anoxic conditions near global whilst the Dienerian–Smithian boundary and the earliest Spathian were better oxygenated intervals. The last two intervals correspond to major, positive carbon isotope perturbations (P2 and P3) and they are separated by a major negative excursion in the late Smithian (N3). Current explanations for all these isotope trends are controversial. P3 is widely regarded to reflect increased productivity and organic C burial as oceanic circulation and upwelling becomes invigorated in a cooling climate. However, geochemical or sedimentological evidence for enhanced anoxia and black shale accumulation slightly predates the peak of P3 suggesting a slight mismatch with the enhanced productivity notion, or potentially the black shales coincident with P3 have yet to be discovered. Alternatively, the P3 excursion may be the result of a calcification crisis and a decline in the proportion of carbon being buried as carbonate relative to organic carbon. Previous studies have noted a dramatic shift from strong positive to weakly negative $\Delta\delta^{13}C_{vert}$ values on transition from N3 to P3 (Song et al., 2013) which are used to invoke the loss of oceanic stratification as upwelling becomes established. Reviewing the currently available data confirms the presence of this change in some regions but its magnitude is substantially less than previously reported.

Comparison of the Qinling Sea $\delta^{13}C_{carb}$ values with elsewhere reveals that, although the usual Early Triassic perturbations are present, the absolute values are a few permil heavier than seen, for example, in the epicontinental basins of South China and are more akin to those of Panthalassan ocean seamounts. We interpret this to reflect the generally more open connection of the Qinling Shelf with the isotopically heavier surface waters of the open ocean. Such connectivity may account for the unusual prevalence of MRBs in the Qinling sections, especially during the Smithian, where advection of deep ferruginous ocean waters was able to supply the Fe needed for their formation. The expansion of MRB formation in the Spathian over wide areas may reflect an increase in overall basin and shelf sea connectivity during a highstand and/or flushing of ferruginous waters from ocean basins during a long-term re-oxygenation event.

Acknowledgments

This work was supported by the National Natural Sciences Foundation of China (grant nos. 41830320, 41572002, 41972033, 41661134047) and China Scholarship Council. We thank Kang Li, Dong Hanxinshuo, Wu Baojin, Zhang Zaitian, Ye Qian, Niu Xiaohong, Song Hong, He Pengfei, Li Linfeng, Ma Haiyuan, Ma Zujun, Li Yongchao, Wang Miaoyan and for their great help in field work and Yi Zhaoyang for later experiments. And thank Chen Yan, Lyu Zhengyi, Peng Zidong for helpful discussion in improving this manuscript.

Figure and Table Captions

Figure 1. The Early Triassic paleogeographic maps (modified from Li et al., 2022). A. Global palaeogeography. B. Regional palaeogeography. Red star denotes Yiwagou section. Abbreviations: YWG = Yiwagou section, SELS = Sai'erlangshan section, SL=Southern Longmenxia section, GBG = Great Bank of Guizhou.

Figure 2. Field photos for Yiwagou section. A–D. Outcrops at the Yiwagou section with bed numbers marked, Yangu Formation (bed -1), Zhalishan Formation (beds 1–19), Maresongduo Formation (beds 20–24). E. Hummocky cross bedding in Mf5, with interpretative sketch. F. Planar lamination in Mf5, with interpretative sketch. G–I. Bedding plane views of trace fossils, coin is 25.75 mm in diameter G. *Lockeia* from Maresongduo Formation, H. *Planolites* from Zhalishan Formation, I. *Skolithos* from Maresongduo Formation.

Figure 3. Thin section images. A–C. Mf1, light grey oolitic grainstone, concentric, bimineralic ooids have alternations of calcite crystal laminae and micritic laminae, B. ooids with isopachous acicular fringe cement and outer calcite crystals, the remaining pores are filled by coarse calcite crystals, A–B from sample YG-029, bed -3, C.

subhedral dolomite crystals replacing ooids, YG-033, bed -3; D–E. brachiopod-gastropod-peloid pack-grainstone of Mf2, sample YG-12, bed -2; F–H. Mf3, F–G. red gastropod-bivalve packstone, fossil fragments have micritic envelopes, sample ZLSO-25, bed 3, H. dark grey gastropod-bivalve packstone, cortoids with bioclasts at the core, sample ZLSO-29, bed 4; I. Mf4, grey bioclastic wackestone, shows a microgastropod, sample ZLS-51, bed 15.

Figure 4. Thin section images. A–G. Mf5, A, E–G. red calcarenites packstone/grainstone with common angular intraclasts, some grains are covered by unequal-thickness acicular aragonitic (?) cements (yellow arrows in E), while others are directly cemented by blocky crystals, E. foraminifer *Agathammina austroalpina*, F. foraminifer *Glomospirella spirillinoides*, red arrows denote possible detrital iron oxide grains, A from sample ZLS-70, bed 15, E from sample ZLS-82, bed 16, F from sample ZLS-83, bed 16, G from sample ZLS-99, bed 17, B–C, red oolitic grainstone, the matrix shows a thick, isopachous rim cement with spar occluding the central cavities, sample ZLS-72, bed 15, D. grey oolitic grainstone, sample ZLS-44, bed 15; H − I. Mf6, H. grey ostracode wackestone, sample 2ZLS-31, bed 18, I. red ostracode-peloidal packstone, sample 2ZLS-29, bed 18; J. Mf7, light grey crystalline dolostone, with subhedral crystals, sample M-20, bed 18; K − L. Mf8, red peloidal packstone, K. foraminifer *Glomospirella vulgaris* from sample MRSD-1, bed 24, L from sample MRSD-2, bed 24.

Figure 5. Yiwagou section showing lithologic log, conodont zones, number of conodont elements per sample (each weighing 4–5 kg, data from Li et al., 2022),

occurrence of other taxa, microfacies, sample numbers, box-and-whisker plots of framboid diameters, carbonate carbon isotope records. Abbreviations: *H.* = *Hindeodus*, *E.* = *Eurygnathodus*, *Nv.* = *Novispathodus*, *Ns.* = *Neospathodus*, *T.* = *Triassospathodus*, *Sc.* = *Scythogondolella*.

Figure 6. Wilkin Plot: mean diameter versus standard deviation plot of pyrite framboid sizes from Yiwagou, see figure 4 for sample heights. The dashed line is derived from (Bond and Wignall, 2010).

Figure 7. Latest Permian to Early Triassic carbon isotope records from Yiwagou, anoxic global seafloor area, marine red beds and redox history chart derived from different regions. Subdivisions of four substage are based on ammonoid biostratigraphy (Dai et al., 2023 and its references). The numeric ages for the Changhsingian–Griesbachian are from Burgess et al. (2014), the Griesbachian–Dienerian boundary (Ovtcharova et al., 2015), the Dienerian–Smithian boundary (Widmann et al., 2020; Dai et al., 2023b), the Smithian–Spathian boundary (Widmann et al., 2020). Model estimates of fractional anoxic global seafloor area (*f* anoxic) are based on the $\delta^{238}U$ records, 1 from (Zhang et al., 2020), 2 from (Cui et al., 2021), 3 from (Zhao et al., 2020a), 4 from (Zhang et al., 2019b). Marine red beds are carbonates (A–F), chert (I) and siliceous claystone (J). A–D. Eastern Tethys, A–B. Qinling shelf sea, A. Sai'erlangshan (Chen, 2020; Xiao et al., 1992), B. Yiwagou (this study), C. Northern Yangtze Platform, showing shallow (Xiejiacao, Zhu et al., 2012), intermediate/deep (Meishan, West Pingdingshan, South Majiashan, Huang et al.,

2017), D. Nanpanjiang Basin, intermediate (Bianyang, Mingtang, Tian et al., 2014; Sun et al., 2015) and deep (Jiarong, Sun et al., 2015); E. Western Tethys, Italy (Wignall and Hallam, 1992; Wignall and Twitchett, 2002; Foster et al., 2017); F–H. Neo-Tethys, F. South Tibet (Wignall and Newton, 2003; Li et al., 2019a), intermediate (Tulong, Selong) and deep (Xiukang), G. Spiti, India (Sun et al., 2021), H. Arabian Margin (Clarkson et al., 2016); I–J. Panthalassa Ocean, I. New Zealand (Grasby et al., 2021), J. Japan (Takahashi et al., 2009, 2014, 2015; Wignall et al., 2010); K–L. Boreal, K. Spitsbergen shelf (Wignall et al., 2016), L. Sverdrup Basin, Arctic Canada (Grasby et al., 2012). Abbreviations: S. = shallow, I. = intermediate, D. = deep.

Figure 8. Raman images. A. Inner part of a red ooid showing iron oxide (purple) organic matter (red), quartz (blue), cryolite (orange) and rutile (light grey), sample ZLS-72; B. inner part of a red, angular intraclast, showing nanometer to micrometer-sized iron oxides, with a few micrometer-sized cryolite grains, sample ZLS-83; C. grey biocalstic packstone, showing pyrite areas (yellow) that have been largely oxidized to iron oxides, also with organic matter, sample ZLS-19; D. raman spectra of the minerals present in A–C. Iron oxides are commonly goethite, but with occasional hematite.

Figure 9. Schematic model for evolution of Qinling Shelf Sea during the Smithian to Spathian. A–B. Shelf carbonates experience substantial storm activity during warming episode, increasing advection of ferruginous ocean waters from adjoining

Paleo-tethys Ocean promoted the deposition of MRBs; C. cooling trend is associated with a cessation of MRB formation, increased productivity and organic matter remineralization within the sediments producing framboids within the dysoxic platform sediments; D. resumption of advection of ferruginous ocean waters into mid shelf areas and development of MRBs.

Figure 10. Comparison of carbon isotope records. Data sources: Yiwagou, South Qinling Platform (Li et al., 2022); Guandao, Nanpanjiang Basin (Payne et al., 2004); Meishan (black from Shen et al., 2013; blue from Song et al., 2013) and West Pingdingshan (black from Tong and Zhao, 2011; blue from Lyu et al., 2019), Northern Yangtze Plarform; Mud, India, (black from Sun et al., 2021; blue from Krystyn et al., 2007).

Figure 11. Compilation of carbon isotope values during the P2, N3, P3 excursions, and the magnitude of the P2–N3 negative and N3–P3 positive excursions derived from $\delta^{13}C_{carb}$ records (54 records in total, Appendix A). Estimated water-depth of sections are divided into shallow, intermediate and deep ranges; water depth information is mainly from Song et al. (2013) and Li et al. (2018).

Figure 12. The $\delta^{13}C$ gradient from shallow- to deep-water sections in three settings at the peak of the P2, N3 and P3 CIEs in the early Triassic (data sources are listed in Appendix A). The P2 $\Delta\delta^{13}C_{vert}$ is positive in Nanpanjiang Basin and Lower Yangtze Basin, but negative in Arabian Margin. The P3 $\Delta\delta^{13}C_{vert}$ is negative in Nanpanjiang Basin and Arabian Margin, but positive in Lower Yangtze Basin. The red star denotes

Yiwagou values from the Qinling Shelf Sea. The P3 value denoted by "?" is from the Lekang section where the $\delta^{13}C$ value is questionable (cf., Tong et al., 2007).

Table 1. Microfacies and depositional settings for the uppermost Permian and Lower Triassic succession of Yiwagou section.

Appendices. Supplementary data

A. Summary of P2, N3, P3 values, P2–N3 negative and N3–P3 positive excursions derived from $\delta^{13}C_{carb}$ records in the world.

B. Analysis of the peak values of the P2, N3 and P3 CIEs in different water depth.

C. Analysis of the peak values of the P2, N3 and P3 CIEs in different regions.

D. Size distributions of the pyrite framboids at Yiwagou section. Abbreviations: D = mean diameter of the framboids (μm); SD = standard deviation of the measurements; n = numbers.

References

Bond, D.P.G., Wignall P.B., 2010. Pyrite framboid study of marine Permian–Triassic boundary sections: a complex anoxic event and its relationship to contemporaneous mass extinction. Geol. Soc. Am. Bull. 122, 1265–1279.

Bond, D.P.G., Wignall P.B., Wang, W., Izon, G., Jiang, H.S., Lai, X.L., Sun, Y.D., Newton, R.J., Shao, L.Y., Vedrine, S., Cope, H., 2010. The mid-Capitanian (Middle Permian) mass extinction and carbon isotope record of South China.

Palaeogeogr., Palaeoclimatol., Palaeoecol. 292, 282–294.

Brayard, A., Bylund, K.G., Jenks, J.F., Stephen, D.A., Olivier, N., Escarguel, G., Fara, E., Vennin, E., 2013. Smithian ammonoid faunas from Utah: implications for Early Triassic biostratigraphy, correlation and basinal paleogeography. Swiss J. Palaeontol. 132, 141–219.

Brühwiler, T., Goudemand, N., Galfetti, T., Bucher, H., Baud, A., Ware, D., Hermann, E., Hochuli, P.A., Martini, R., 2009. The Lower Triassic sedimentary and carbon isotope records from Tulong (South Tibet) and their significance for Tethyan palaeoceanography. Sediment. Geol. 222, 314–332.

Cai, Y.F., Hu, X.X., Li, X., Pan, Y.G., 2012. Origin of the red colour in a red limestone from the Vispi Quarry section (central Italy): A high-resolution transmission electron microscopy analysis. Cretaceous Res. 38, 97–102.

Chen, Y., 2020. Magnetostratigraphy timescale in South China during the Paleozoic-Mesozoic upheavals and its global correlation, PhD. Thesis. China University of Geosciences, Wuhan, 172p. (in Chinese)

Chen, B., Joachimski, M.M., Shen, S.Z., Lambert, L.L., Lai, X.L., Wang, X.D., Chen, J., Yuan, D.X., 2013. Permian ice volume and palaeoclimate history: Oxygen isotope proxies revisited. Gondwana Res. 24, 77–89.

Clarkson, M.O., Wood, R.A., Poulton, S.W., Richoz, S., Newton, R.J., Kasemann, S.A., Bowyer, F., Krystyn, L., 2016. Dynamic anoxic ferruginous conditions during the end-Permian mass extinction and recovery. Nat. Comms. 7, 10.1038/ncomms12236

Cui, Y., Zhang, F.F., Wang, J.Y., Jiang, S.J., Shen, S.Z., 2021. Marine Anoxia and Ocean Acidification During the End-Permian Extinction: An Integrated View From $\delta^{238}U$ and $\delta^{44/40}Ca$ Proxies and Earth System Modeling, in: Ernst, R.E., Dickson, A.J., Bekker, A., (Eds.), Large Igneous Provinces: A Driver of Global Environmental and Biotic Changes, Geophysical Monograph 255, 325–340.

Dai, X., Yuan, Z.W., Brayard, A., Li, M.T., Liu, X.K., Jia, E.H., Du, Y., Song, H.Y., Song, H.J., 2021. Calibrating the late Smithian (Early Triassic) crisis: New insights from the Nanpanjiang Basin, South China. Glob. Planet. Change, 201, 103492.

Du, Y., Song, H.Y., Algeo, T.J., Song, H.J., Tian, L., Chu, D.L., Shi, W., Li, C., Tong, J.N., 2022. A massive magmatic degassing event drove the Late Smithian Thermal Maximum and Smithian–Spathian boundary mass extinction. Glob. Planet. Change, 215, 103878.

Feng, Q.L., Du, Y.S., Zhang, Z.H., Zeng, X.Y., 1994. Early Triassic radiolarian fauna of Tongbai region in Henan and its geologic significance: Earth Sci. 19, 787–794. (in Chinese)

Foster, W.J., Danise, S., Price, G.D., Twitchett, R.J., 2017. Subsequent biotic crises delayed marine recovery following the late Permian mass extinction event in northern Italy. PLOS ONE. 12, e0172321-e0172321.

Galfetti, T., Hochuli, P.A., Brayard, A., Bucher, H., Weissert, H., Vigran, J.O., 2007. Smithian–Spathian boundary event: Evidence for global climate change in the wake of the end-Permian biotic crisis. Geology, 35, 291–294.

Galfetti, T., Bucher, H., Martini, R., Hochuli, P.A., Weissert, H., Crasquin-Soleau, S., Brayard, A., Goudemand, N., Brühwiler, T., Guodun, K., 2008. Evolution of Early Triassic outer platform paleoenvironments in the Nanpanjiang Basin (South China) and their significance for the biotic recovery. Sediment. Geol. 204, 36–60.

Gledhill, M., Buck, K.N., 2012. The organic complexation of iron in the marine environment: a review, Front. Microbiol. 3, 1–17.

Goudemand, N., Romano, C., Leu, M., Bucher, H., Trotter, J.A., Williams, I.S., 2019. Dynamic interplay between climate and marine biodiversity upheavals during the early Triassic Smithian–Spathian biotic crisis. Earth-Sci. Rev. 195, 169–178.

Grasby, S.E., Beauchamp, B., Embry, A., Sanei, H., 2012, Recurrent Early Triassic ocean anoxia. Geology, 41, 175–178.

Grasby, S.E., Beauchamp, B., Bond, D.P.G., Wignall, P.B., Sanei, H., 2016. Mercury anomalies associated with three extinction events (Capitanian crisis, latest Permian extinction and the Smithian/Spathian extinction) in NW Pangea. Geol. Mag. 153, 285–297.

Grasby, S.E., Bond, D.P.G., Wignall, P.B., Yin, R., Strachan, L.J., Takahashi, S., 2021. Transient Permian–Triassic euxinia in the southern Panthalassa deep ocean. Geology, 49, 889–893.

Hallam, A., 1992. Why was there a delayed radiation after the end-Palaeozoic crisis? Historical Biology, 5, 257–262.

Hammer, Ø., Jones, M.T., Schneebeli-Hermann, E., Hansena, B.B., Bucher, H., 2019. Are Early Triassic extinction events associated with mercury anomalies? A reassessment of the Smithian/Spathian boundary extinction. Earth-Sci. Rev. 195, 179–190.

Horacek, M., Richoz, S., Brandner, R., Krystyn, L., Spötl, C., 2007. Evidence for recurrent changes in Lower Triassic oceanic circulation of the Tethys: the $\delta^{13}C$ record from marine sections in Iran. Palaeogeogr., Palaeoclimatol., Palaeoecol. 252, 355–369.

Hu, X.M., Scott, R.W., Cai, Y.F., Wang, C.S., Melinte-Dobrinescu, M.C., 2012. Cretaceous oceanic red beds (CORBs): different time scales and models of origin. Earth-Sci. Rev. 115, 217–248.

Huang, Y.G., Chen, Z.Q., Wignall, P.B., Zhao, L.S., 2017. Latest Permian to Middle Triassic redox condition variations in ramp settings, South China: Pyrite framboid evidence. Geol. Soc. Am. Bull. 129, 229–243.

Immenhauser, A., Della Porta, G., Kenter, J.A.M., Bahamonde, J.R., 2003. An alternative model for positive shifts in shallow-marine carbonate $\delta^{13}C$ and $\delta^{18}O$. Sedimentology, 50, 953–959.

Joachimski, M.M., Lai, X.L., Shen, S.Z., Jiang, H.S., Luo, G.M., Chen, B., Chen, J., Sun, Y.D., 2012. Climate warming in the latest Permian and the Permian–Triassic mass extinction. Geology, 40, 195–198.

Krystyn, L., Richoz S., Bhargava, O.N., 2007. The Induan-Olenekian Boundary (IOB) in Mud – an update of the candidate GSSP section M04. Albertiana, 36, 33–45.

Lai, X.L., 1992. Conodont, in: Yin, H.F., Yang, F.Q., Huang, Q.S., Yang, H.S., Lai, X.L. (Eds.), Triassic in Qinling and Adjacent Areas. China University of Geosciences Press, Wuhan, 66–68 (in Chinese).

Lai, X.L., Xu, X.R., 1992. Early Triassic lithofacies and biofacies in South Qinling, in: Yin, H.F., Yang, F.Q., Huang, Q.S., Yang, H.S., Lai, X.L. (Eds.), Triassic in Qinling and adjacent areas. China University of Geosciences Press, Wuhan, 96–103 (in Chinese).

Lai, X.L., Yin, H.F., Yang, F.Q., 1992. The character and evolution of ecostratigraphy and paleobiogeography of Triassic Qinling Basin. Earth Sci. 17, 345–352 (in Chinese with English abstract).

Lai, X.L., Yang, F.Q., Yin, H.F., 1994. Research on Permian–Triassic boundary strata, in west Qinling Area. Geoscience. 8, 20–26 (in Chinese with English abstract).

Lai, X.L., Yin, H.F., and Yang, F.Q., 1995. Reconstruction of the Qinling Triassic Paleo-ocean: Earth Sci. 20, 648–656 (in Chinese).

Li, M.T., Song, H.J., Algeo, T.J., Wignall, P.B., Dai, X., Woods, A.D., 2018. A dolomitization event at the oceanic chemocline during the Permian–Triassic transition. Geology, 46, 1043–1046.

Li, M.T., Song, H.J., Wignall, P.B., She, Z.B., Dai, X., Song, H.Y., Xiao, Q., 2019a. Early Triassic oceanic red beds coupled with deep sea oxidation in South Tethys. Sediment. Geol. 391, 105519.

Li, M.T., Wignall, P.B., Dai, X., Hu, M.Y., Song, H.J., 2021. Phanerozoic variation in dolomite abundance linked to oceanic anoxia. Geology, 49, 698–702.

Li, F., Yan, J.X., Chen, Z.Q., Ogg, J.G., Tian, L., Korngreen, D., Liu, K., Ma, Z.L., Woods, A.D., 2015. Global oolite deposits across the Permian–Triassic boundary: A synthesis and implications for palaeoceanography immediately after the end-Permian biocrisis. Earth-Sci. Rev. 149, 163–180.

Li, H.X., Jiang, H.S., Chen, Y.L., Wignall, P.B., Wu, B.J., Zhang, Z.T., Zhang, M.H., Ouyang, Z.M., Lai, X.L., 2019b. Smithian platform-bearing gondolellid conodonts from Yiwagou Section, northwestern China and implications for their geographic distribution in the Early Triassic. J. Paleontol. 93, 496–511.

Li, H.X., Dong, H.X.S., Jiang, H.S., Wignall, P.B., Chen, Y.L., Zhang, M.H., Ouyang, Z.M., Wu, X.L., Wu, B.J., Zhang, Z.T., Lai, X.L., 2022. Integrated conodont biostratigraphy and $\delta^{13}C_{carb}$ records from end Permian to Early Triassic at Yiwagou Section, Gansu Province, northwestern China and their implications. Palaeogeogr., Palaeoclimatol., Palaeoecol. 601, 111079.

Lyu, Z.Y., Zhang, L., Algeo, T.J., Zhao, L.S., Chen, Z.Q., Li, C., Ma, B., Ye, F.H., 2019. Global-ocean circulation changes during the Smithian–Spathian transition inferred from carbon-sulfur cycle records. Earth-Sci. Rev. 195, 114–132.

Matheson, E.J., Pufahl, P.K., Voinot, A., Murphy, J.B., Fitzgerald, D.M., 2022. Ironstone as a proxy of Paleozoic ocean oxygenation. Earth Planet. Sci. Lett. 594, 117715.

Metcalfe, I., 2013. Gondwana dispersion and Asian accretion: Tectonic and palaeogeographic evolution of eastern Tethys. J. Asian Earth Sci. 66, 1–33.

Meyer, K.M., Yu, M., Jost, A.B., Kelley, B.M., Payne, J.L., 2011. $\delta^{13}C$ evidence that high primary productivity delayed recovery from end-Permian mass extinction. Earth Planet. Sci. Lett. 302, 378–384.

Muttoni, G., Gaetani, M., Kent, D.V., Sciunnach, D., Angiolini, L., Berra, F., Garzanti, E., Mattei, M., Zanchi, A., 2009. Opening of the Neo-Tethys Ocean and the Pangea B to Pangea A transformation during the Permian. GeoArabia, 14, 17–48.

Orchard, M.J., 2007. Conodont diversity and evolution through the latest Permian and Early Triassic upheavals. Palaeogeogr., Palaeoclimatol., Palaeoecol. 252, 93–117.

Patterson, W.P., Walter, L.M., 1994. Depletion of ^{13}C in seawater ΣCO_2 on modern carbonate platforms: Significance for the carbon isotopic record of carbonates. Geology, 22, 885–888.

Payne, J.L., Kump, L.R., 2007. Evidence for recurrent Early Triassic massive volcanism from quantitative interpretation of carbon isotope fluctuations. Earth Planet. Sci. Lett. 256, 264–277.

Payne, J.L., Lehrmann, D.J., Wei, J.Y., Orchard, M.J., Schrag, D.P., Knoll, A.H., 2004. Large perturbations of the carbon cycle during recovery from the end-Permian extinction. Science, 305, 506–509.

Romano, C., Goudemand, N., Vennemann, T.W., Ware, D., Schneebeli-Hermann, E., Hochuli, P.A., Brühwiler, T., Brinkmann, W., Bucher, H., 2013. Climatic and biotic upheavals following the end-Permian mass extinction. Nat. geoscience, 6, 57–60.

Shen, J., Algeo, T.J., Planavsky, N.J., Yu, J.X., Feng, Q.L., Song, H.J., Song, H.Y., Rowe, H., Zhou, L., Chen, J.B., 2019. Mercury enrichments provide evidence of Early Triassic volcanism following the end-Permian mass extinction. Earth-Sci. Rev. 195, 191–212.

Shen, S.Z., Cao, C.Q., Zhang, H., Bowring, S.A., Henderson, C.M., Payne, J.L., Davydov, V.I., Chen, B., Yuan, D.X., Zhang, Y.C., Wang, W., Zheng, Q.F., 2013. High-resolution $\delta^{13}C_{carb}$ chemostratigraphy from latest Guadalupian through earliest Triassic in South China and Iran. Earth Planet. Sci. Lett. 375, 156–165.

Song, H.J., Jiang, G.Q., Poulton, S.W., Wignall, P.B., Tong, J.N., Song, H.Y., An, Z.H., Chu, D.L., Tian, L., She, Z.B., Wang, C.S., 2017. The onset of widespread marine red beds and the evolution of ferruginous oceans. Nat. Comms. 8, 399.

Song, H.J., Kemp, D.B., Tian, L., Chu, D.L., Song, H.Y., Dai, X., 2021a. Thresholds of temperature change for mass extinctions. Nat. Comms. 12, 4694–4694.

Song, H.J., Song, H.Y., Tong, J.N., Gordon, G.W., Wignall, P.B., Tian, L., Zheng, W., Algeo, T.J., Liang, L., Bai, R.Y., Wu, K., Anbar, A.D. 2021b. Conodont calcium isotopic evidence for multiple shelf acidification events during the early Triassic. Chem. Geol. 562, 120038.

Song, H.Y., Tong, J.N., Algeo, T.J., Horacek, M., Qiu, H.O., Song, H.J., Tian, L., Chen, Z. Q., 2013. Large vertical $\delta^{13}C_{DIC}$ gradients in Early Triassic seas of the South China craton: implications for oceanographic changes related to Siberian Traps volcanism. Glob. Planet. Change, 105, 7–20.

Song, H.Y., Du, Y., Algeo, T.J., Tong, J.N., Owens, J.D., Song, H.J., Tian, L., Qiu, H.O., Zhu, Y.Y., Lyons, T.W., 2019. Cooling-driven oceanic anoxia across the Smithian/ Spathian boundary (mid-early Triassic). Earth-Sci. Rev. 195, 133–146.

Stanley, S.M., 2009. Evidence from ammonoids and conodonts for multiple Early Triassic mass extinctions. Proc. Nat. Acad. Sci., 106, 15264–15267.

Stebbins, A., Algeo, T.J., Krystyn, L., Rowe, H., Brookfield, M., Williams, J., Nye, S.W., Hannigan, R., 2018. Marine sulfur cycle for upwelling and eutrophic stress during Early Triassic cooling events. Earth-Sci. Rev., 195, 68–82.

Sun, Y.D., Joachimski, M.M., Wignall, P.B., Yan, C.B., Chen, Y.L., Jiang, H.S., Wang, L.N., Lai, X.L., 2012. Lethally hot temperatures during the Early Triassic greenhouse. Science, 338, 366–370.

Sun, Y.D., Wignall, P.B., Joachimski, M.M., Bond, D.P.G., Grasby, S.E., Sun, S., Yan, C.B., Wang, L.N., Chen, Y.L., Lai, X.L., 2015. High amplitude redox changes in the late Early Triassic of South China and the Smithian–Spathian extinction. Palaeogeogr., Palaeoclimatol., Palaeoecol. 427, 62–78.

Sun, Y.D., Richoz, S., Krystyn, L., Grasby, S.E., Chen, Y.L., Banerjee, D., Joachimski, M.M., 2021. Integrated bio-chemostratigraphy of Lower and Middle

Triassic marine successions at Spiti in the Indian Himalaya: implications for the Early Triassic nutrient crisis. Glob. Planet. Change, 196, 103363.

Takahashi, S., Masahiro, O., Kunio, K., Satoshi, Y., Susumu, S., 2009. Panthalassic oceanic anoxia at the end of the Early Triassic: A cause of delay in the recovery of life after the end-Permian mass extinction. Palaeogeogr., Palaeoclimatol., Palaeoecol. 274, 185–195.

Takahashi, S., Yamasaki, S., Ogawa, Y., Kimura, K., Kaiho, K., Yoshida, T., Tsuchiya, N., 2014. Bioessential element-depleted ocean following the euxinic maximum of the end-Permian mass extinction. Earth Planet. Sci. Lett. 393, 94–104.

Takahashi, S., Yamasaki, S., Ogawa, K., Kaiho, K., Tsuchiya, N., 2015. Redox conditions in the end-Early Triassic Panthalassa. Palaeogeogr., Palaeoclimatol., Palaeoecol. 432, 15–28.

Tian, L., Tong, J.N., Algeo, T.J., Song, H.J., Song, H.Y., Chu, D.L., Shi, L., Bottjer, D.J., 2014. Reconstruction of Early Triassic ocean redox conditions based on framboidal pyrite from the Nanpanjiang Basin, South China. Palaeogeogr., Palaeoclimatol., Palaeoecol. 412, 68–79.

Tong, J.N., Zuo, J.X., Chen, Z.Q., 2007. Early Triassic carbon isotope excursions from South China: Proxies for devastation and restoration of marine ecosystems following the end-Permian mass extinction. Geol. J. 42, 371–389.

Tong, J.N., Zhao, L.S., 2011. Lower Triassic and Induan-Olenekian boundary in Chaohu, Anhui Province, South China. Acta Geol. Sin. 85, 399–407.

Widmann, P., Bucher, H., Leu, M., Vennemann, T., Bagherpour, B., Schneebeli-Hermann, E., Goudemand, N., Schaltegger, U., 2020. Dynamics of the largest carbon isotope excursion during the Early Triassic biotic recovery. Front. Earth Sci. 8, https://doi.org/10.3389/feart.2020.00196

Wignall, P.B., Hallam, A., 1992. Anoxia as a cause of the Permian/Triassic mass extinction: facies evidence from northern Italy and the western United States. Palaeogeogr., Palaeoclimatol., Palaeoecol., 93, 21–46.

Wignall, P.B., Newton, R., 2003. Contrasting deep-water records from the Upper Permian and Lower Triassic of South Tibet and British Columbia: Evidence for a diachronous aass extinction. Palaios, 18, 153–167.

Wignall, P.B., Twitchett, R.J., 2002. Permian–Triassic sedimentology of Jameson Land, East Greenland: incised submarine channels in an anoxic basin. J. Geol. Soc. 159, 691–703.

Wignall, P.B., Morante, R., Newton, R., 1998. The Permo-Triassic transition in Spitsbergen: $\delta^{13}C_{org}$ chemostratigraphy, Fe and S geochemistry, facies, fauna and trace fossils. Geol. Mag. 135, 47–62.

Wignall, P.B., Bond, D.P.G., Kuwahara, K., Kakuwa, Y., Newton, R.J., Poulton, S.W., 2010. An 80 million year oceanic redox history from Permian to Jurassic pelagic sediments of the Mino-Tamba terrane, SW Japan, and the origin of four mass extinctions. Glob. Planet. Change, 71, 109–123.

Wignall, P.B., Bond, D.P.G., Sun, Y.D., Grasby, S.E., Beauchamp, B., Joachimski, M.M., Blomeier, D.P.G., 2016. Ultra-shallow-marine anoxia in an Early Triassic shallow-marine clastic ramp (Spitsbergen) and the suppression of benthic radiation. Geol. Mag., 153, 316–331.

Wilkin, R.T., Barnes, H.L., Brantley, S.L., 1996. The size distribution of framboidal pyrite in modern sediments: An indicator of redox conditions. Geochim. Cosmochim. Acta, 60, 3897–3912.

Woods, A.D., 2013. Microbial ooids and cortoids from the Lower Triassic (Spathian) Virgin Limestone, Nevada, USA: Evidence for an Early Triassic microbial bloom in shallow depositional environments. Glob. Planet. Change, 105, 91–101.

Xiao, C.T., Yang, H.S., Wu, L.F., 1992. Sai'erlangshan Section in Zoigê, Sichuan Province, in: Yin, H.F., Yang, F.Q., Huang, Q.S., Yang, H.S., Lai, X.L. (Eds.), Triassic in Qinling and adjacent areas. China University of Geosciences Press, Wuhan, 96–103 (in Chinese).

Xie, F.W., Tang, J.X., 2021. The Late Triassic-Jurassic magmatic belt and its implications for the double subduction of the Neo-Tethys Ocean in the southern Lhasa subterrane, Tibet. Gondwana Research, 97, 1–21.

Yang, F.Q., 1992. Trace fossil, in Yin, H.F., Yang, F.Q., Huang, Q.S., Yang, H.S., and Lai, X.L. (Eds.), Triassic in Qinling and adjacent areas. China University of Geosciences Press, Wuhan, 69–72. (in Chinese)

Yin, H.F., Peng, Y.Q., 1995. Evolution of the Phanerozoic Paleo-ocean of Qinling: Earth Sci. 20, 605–611. (in Chinese)

Zhang, L., Zhao, L., Chen, Z.Q., Algeo, T.J., Li, Y., Cao, L., 2015. Amelioration of marine environments at the Smithian–Spathian boundary, Early Triassic. Biogeosciences, 12, 1597–1613.

Zhang, L., Orchard, M.J., Brayard, A., Algeo, T.J., Zhao, L.S., Chen, Z.Q., Lyu, Z.Y., 2019a. The Smithian/Spathian boundary (late Early Triassic): a review of ammonoid, conodont, and carbon-isotopic criteria. Earth-Sci. Rev. 195, 7–36.

Zhang, F.F., Romaniello, S.J., Algeo, T.J., Lau, K.V., Clapham, M.E., Richoz, S., Herrmann, A.D., Smith, H., Horacek, M., Anbar, A.D., 2018. Multiple episodes of extensive marine anoxia linked to global warming and continental weathering following the latest Permian mass extinction. Sci. Adv. 4, e1602921-e1602921

Zhang, F.F., Algeo, T.J., Cui, Y., Shen, J., Song, H.Y., Sano, H., Rowe, H.D., Anbar, A.D., 2019b. Global-ocean redox variations across the Smithian–Spathian boundary linked to concurrent climatic and biotic changes. Earth-Sci. Rev. 195, 147–168.

Zhang, F.F., Shen, S.Z., Cui, Y., Lenton, T.M., Dahl, T.W., Zhang, H., Zheng, Q.F., Wang, W.Q., Krainer, K., Anbar, A.D., 2020a. Two distinct episodes of marine anoxia during the Permian–Triassic crisis evidenced by uranium isotopes in marine dolostones. Geochim. Cosmochim. Acta, 287, 165–179.

Zhang, B.L., Yao, S.P., Mills, B.J.W., Wignall, P.B., Hu, W.X., Liu, B., Ren, Y.L., Li, L.L., Shi, G., 2020b. Middle Permian organic carbon isotope stratigraphy and the origin of the Kamura Event. Gondwana Res., 79, 217–232.

Zhang, G.J., Zhang, X.L., Li, D.D., Jiang, H.S., Xu, Y.L., Li, M.H., Y.N., Shen, 2021. Evidence for the expansion of anoxia during the Smithian from a quantitative interpretation of paired C-isotopes. Glob. Planet. Change, 204, 103551.

Zhao, H., Algeo, T.J., Liu, Y.S., Chen, Z.Q., Zhang, L., Hu, Z.C., Li, Z.H., 2020a. Lower Triassic carbonate $\delta^{238}U$ record demonstrates expanded oceanic anoxia during Smithian Thermal Maximum and improved ventilation during Smithian–Spathian boundary cooling event. Palaeogeogr., Palaeoclimatol., Palaeoecol. 539, 109393.

Zhao, H., Dahl, T.W., Chen, Z.Q., Algeo, T.J., Zhang, L., Liu, Y.S., Hu, Z.C., Hu, Z.H., 2020b. Anomalous marine calcium cycle linked to carbonate factory change after the Smithian Thermal Maximum (Early Triassic). Earth-Sci. Rev. 211, 103418.

Zhu, Y.H., Luo H., Cai H.W., Xu B., Yang H., Zhao Y.Y., Chen D.S., Zhou Z.C., Chen, J.H., 2012. Stratigraphic Division of the Early and Middle Triassic at the Xiejiacao Section in Guang'an, Sichuan. J. Stratigraphy, 4, 784–791 (in Chinese).

Figure1

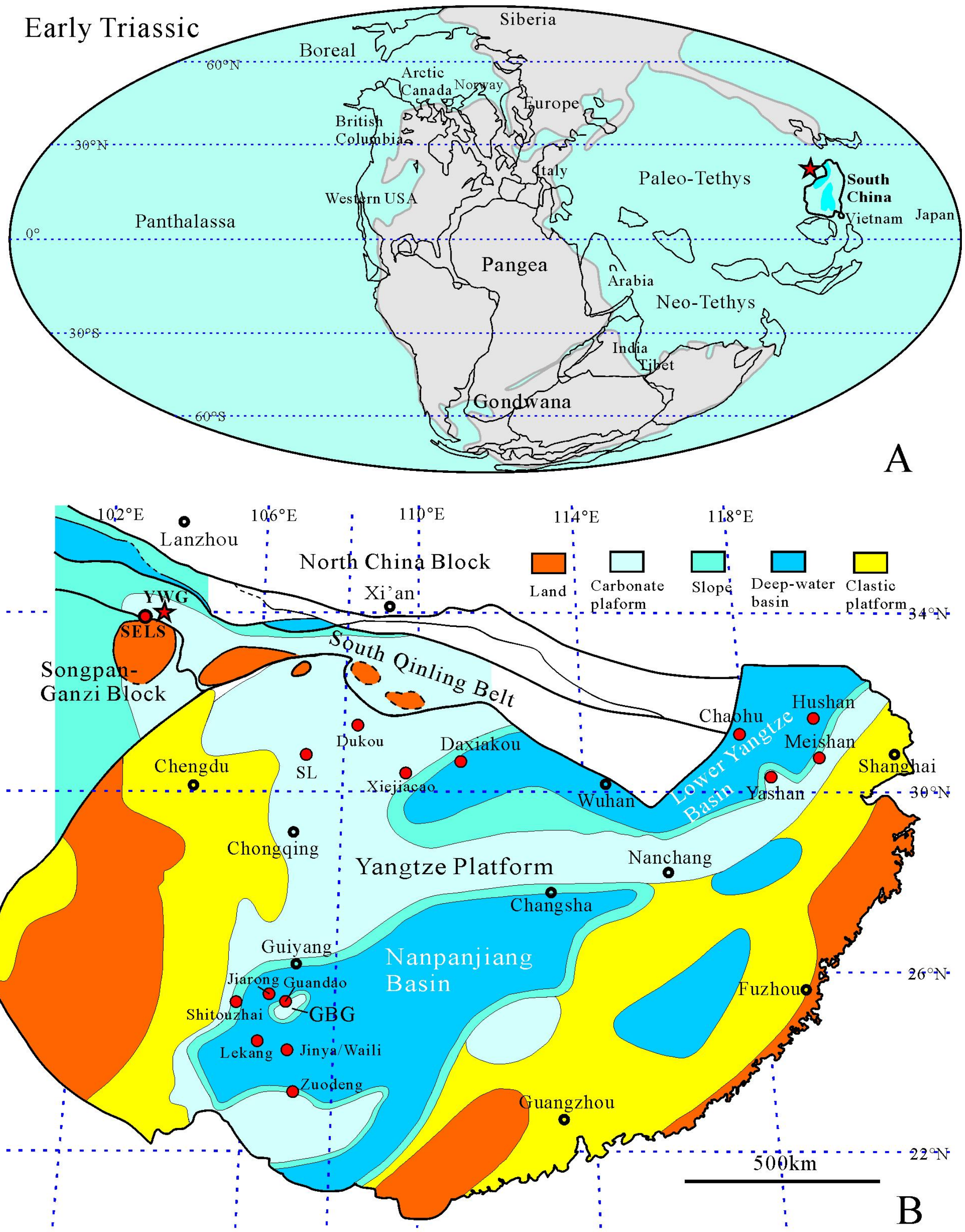
Early Triassic
Boreal
Siberia
60°N
Arctic
Canada
Norway
Europe
British
Columbia
30°N
Italy
Paleo-Tethys
South
China
Western USA
Panthalassa
Vietnam
Japan
0°
Pangea
Arabia
Neo-Tethys
30°S
India
Tibet
Gondwana
60°S
A
102°E
106°E
110°E
114°E
118°E
Lanzhou
North China Block
Land
Carbonate
plaform
Slope
Deep-water
basin
Clastic
platform
Xi'an
YWG
SELS
34°N
South Qinling Belt
Songpan-
Ganzi Block
Chaohu
Hushan
Lower Yangtze
Basin
Meishan
Shanghai
Dukou
Daxiakou
Chengdu
SL
Xiejiacao
Wuhan
Yashan
30°N
Chongqing
Yangtze Platform
Nanchang
Changsha
Guiyang
Nanpanjiang
Basin
Jiarong
Guandao
Shitouzhai
GBG
26°N
Fuzhou
Lekang
Jinya/Waili
Zuodeng
Guangzhou
22°N
500km
B

Figure2

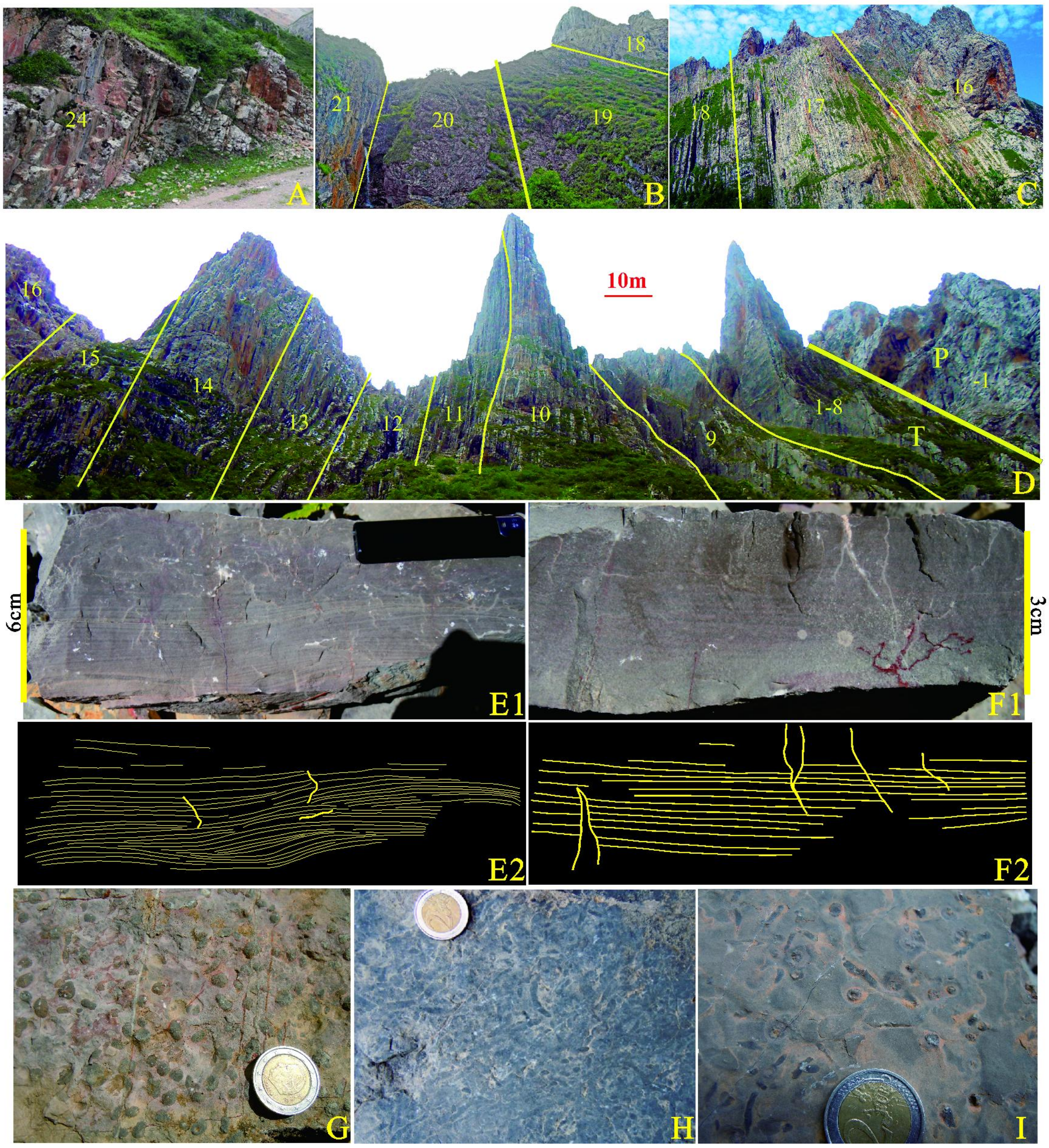

24
A
21
20
19
18
B
18
17
16
C
16
15
14
13
12
11
10
10m
9
1-8
T
P
-1
D
6cm
E1
3cm
F1
E2
F2
G
H
I

Figure3

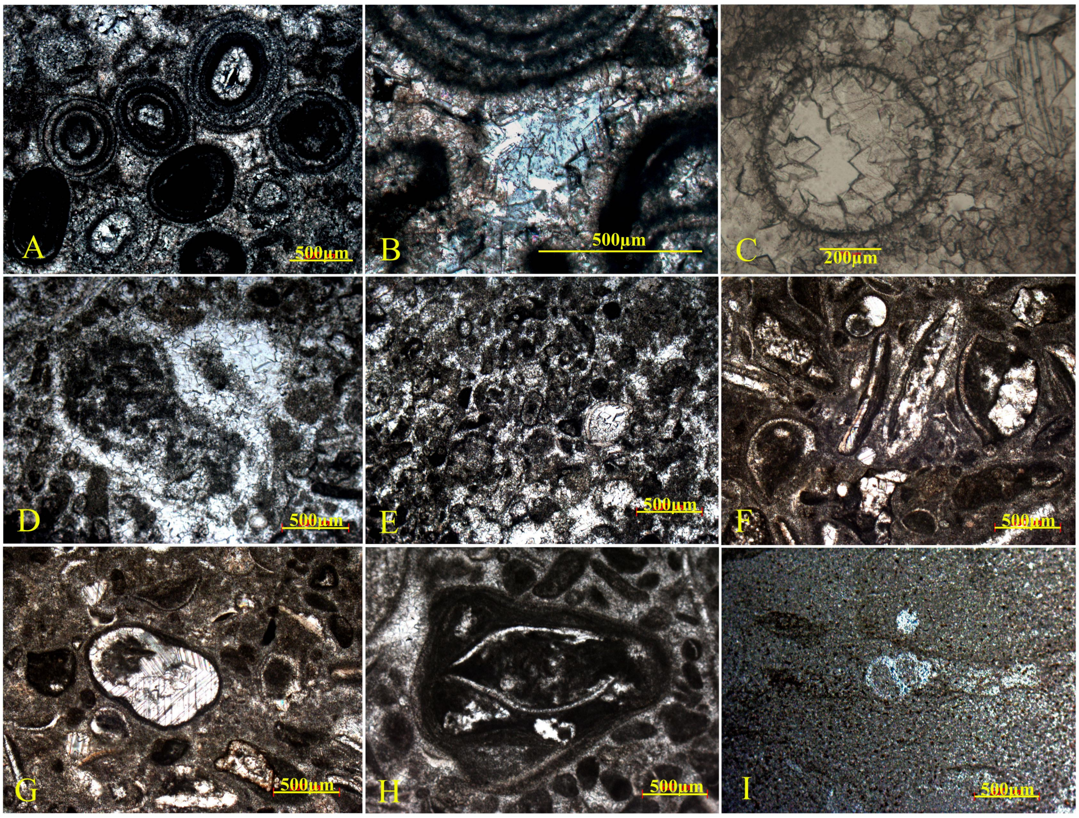
A
500µm
B
500µm
C
200µm
D
500µm
E
500µm
F
500µm
G
500µm
H
500µm
I
500µm

Figure4

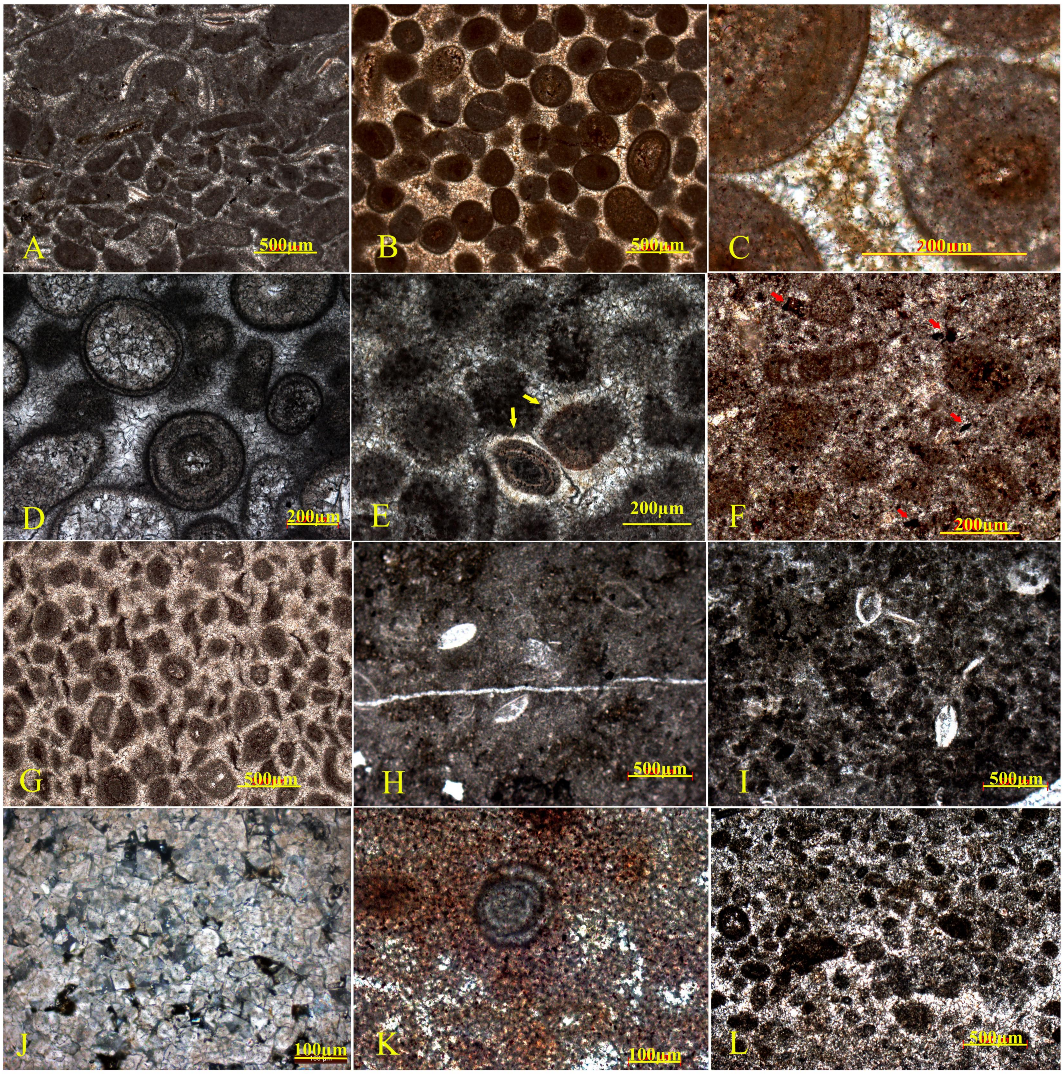
A
500μm
B
500μm
C
200μm
D
200μm
E
200μm
F
200μm
G
500μm
H
500μm
I
500μm
J
100μm
K
100μm
L
500μm

Figure5

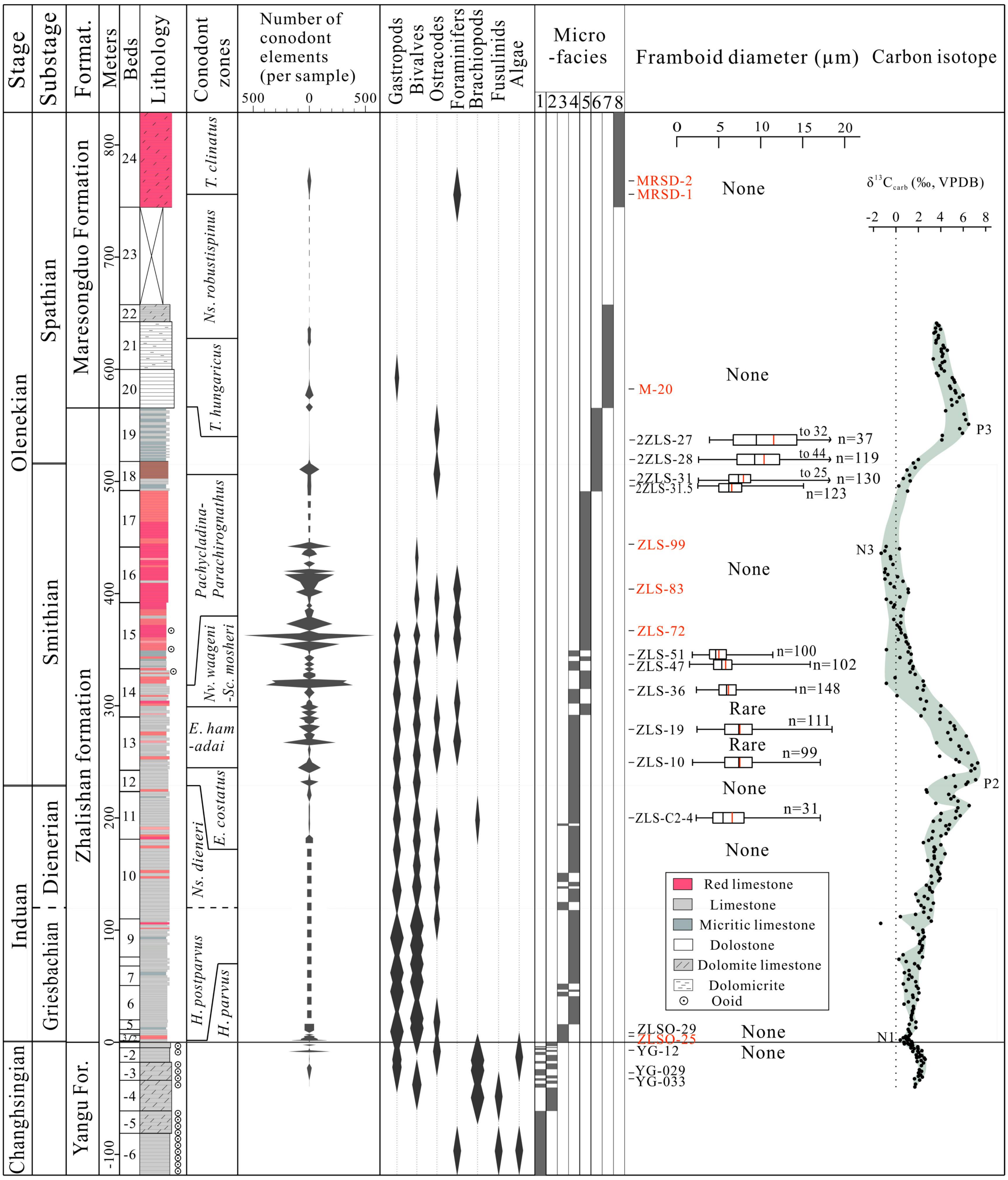

Stage
Substage
Format.
Meters
Beds
Lithology
Conodont zones
Number of conodont elements (per sample)
Gastropods
Bivalves
Ostracodes
Foraminifers
Brachiopods
Fusulinids
Algae
Micro -facies
Framboid diameter (μm)
Carbon isotope
Olenekian
Induan
Changhsingian
Spathian
Smithian
Dienerian
Griesbachian
Maresongduo Formation
Zhalishan formation
Yangu For.
T. clinatus
Ns. robustispinus
T. hungaricus
Pachycladina-Parachirognathus
Nv. waageni -Sc. mosheri
E. ham -adai
Ns. dieneri
E. costatus
H. postparvus
H. parvus
MRSD-2
MRSD-1
M-20
2ZLS-27
2ZLS-28
2ZLS-31
2ZLS-31.5
ZLS-99
ZLS-83
ZLS-72
ZLS-51
ZLS-47
ZLS-36
ZLS-19
ZLS-10
ZLS-C2-4
ZLSO-29
ZLSO-25
YG-12
YG-029
YG-033
None
Rare
n=37
n=119
n=130
n=123
n=100
n=102
n=148
n=111
n=99
n=31
to 32
to 44
to 25
$\delta^{13}C_{carb}$ (‰, VPDB)
P3
P2
N3
N1
Red limestone
Limestone
Micritic limestone
Dolostone
Dolomite limestone
Dolomicrite
Ooid

Figure6

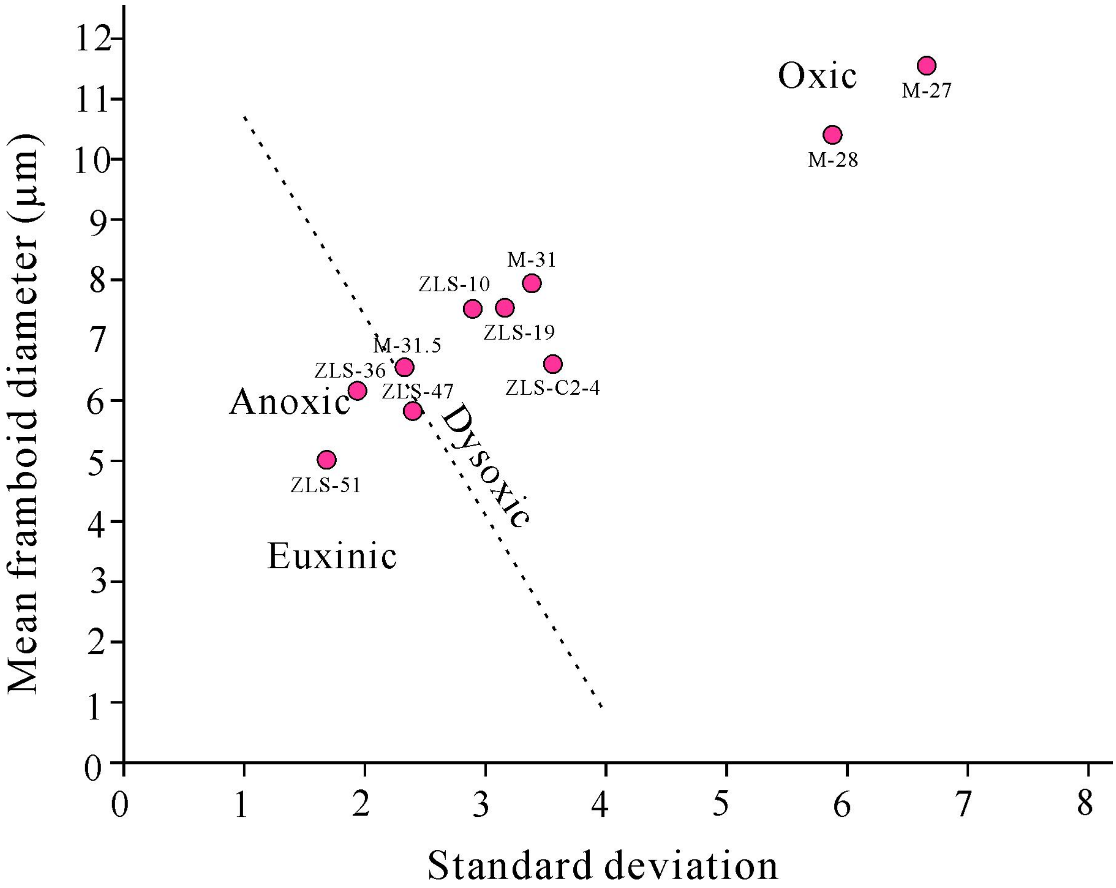
Mean framboid diameter (μm)
Standard deviation
Oxic
Anoxic
Dysoxic
Euxinic
M-27
M-28
M-31
ZLS-10
ZLS-19
M-31.5
ZLS-36
ZLS-47
ZLS-C2-4
ZLS-51
0
1
2
3
4
5
6
7
8
9
10
11
12

Figure7

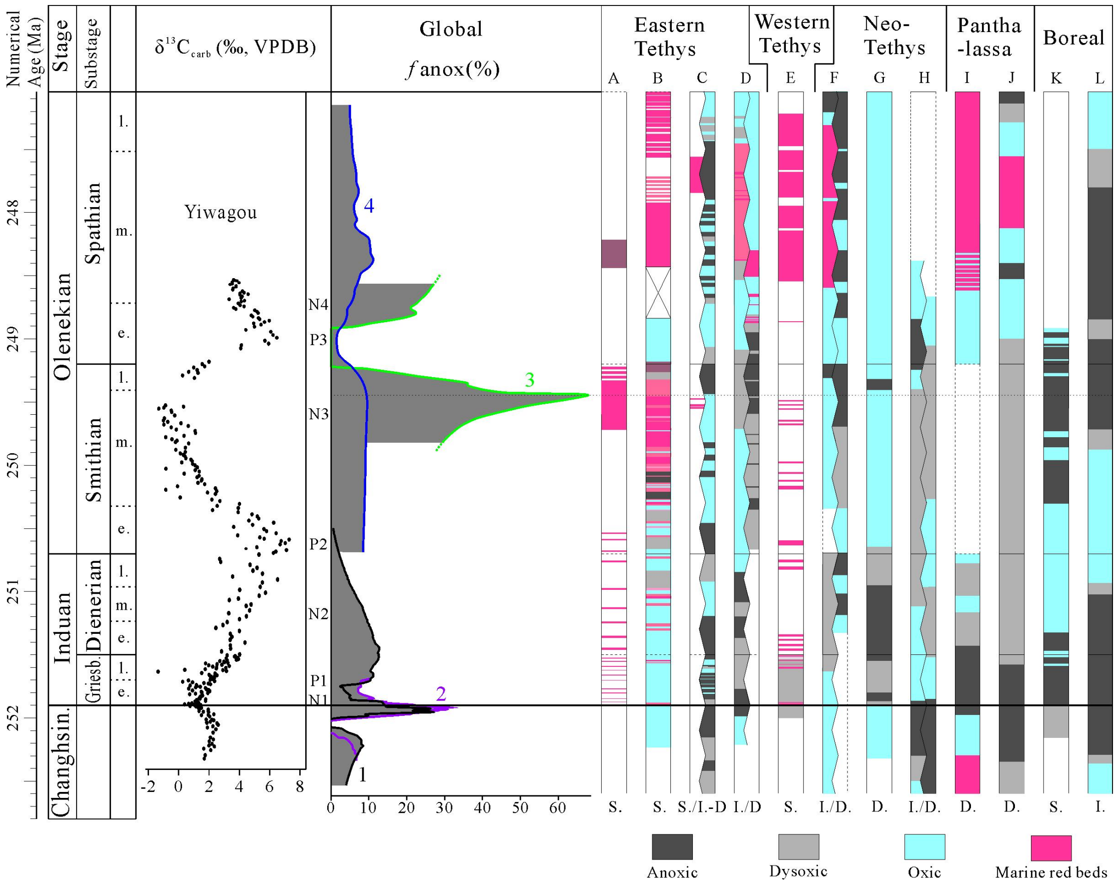

Numerical Age (Ma)
Stage
Substage
δ13Ccarb (‰, VPDB)
Global
ƒanox(%)
Eastern Tethys
Western Tethys
Neo-Tethys
Pantha -lassa
Boreal
A
B
C
D
E
F
G
H
I
J
K
L
248
249
250
251
252
Olenekian
Induan
Changhsin.
Spathian
Smithian
Dienerian
Griesb.
l.
m.
e.
Yiwagou
-2
0
2
4
6
8
N4
P3
N3
P2
N2
P1
N1
1
2
3
4
0
10
20
30
40
50
60
S.
S./I.-D
I./D
I./D.
D.
I./D.
I.
Anoxic
Dysoxic
Oxic
Marine red beds

Figure8

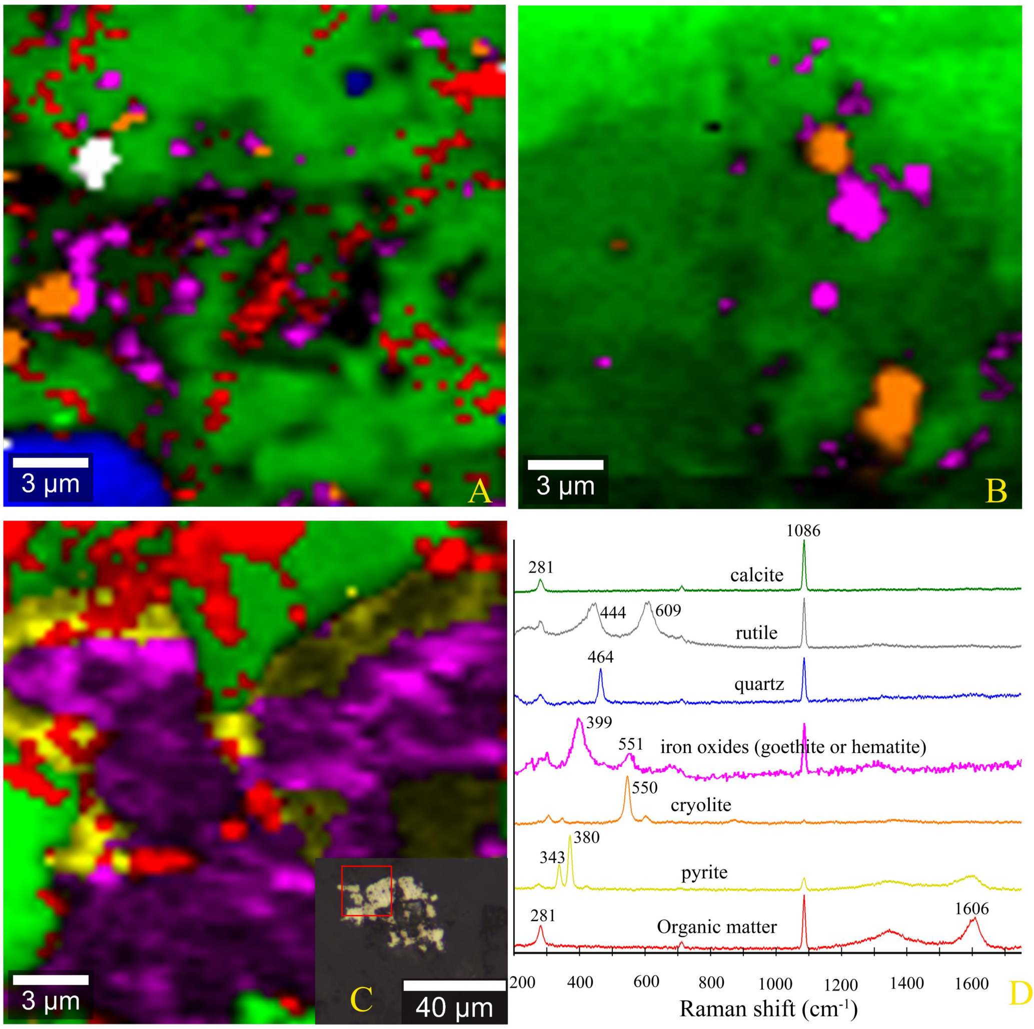
3 µm
A
3 µm
B
3 µm
C
40 µm
D
1086
281
calcite
444
609
rutile
464
quartz
399
551
iron oxides (goethite or hematite)
550
cryolite
380
343
pyrite
281
1606
Organic matter
200
400
600
800
1000
1200
1400
1600
Raman shift (cm-1)

Figure9

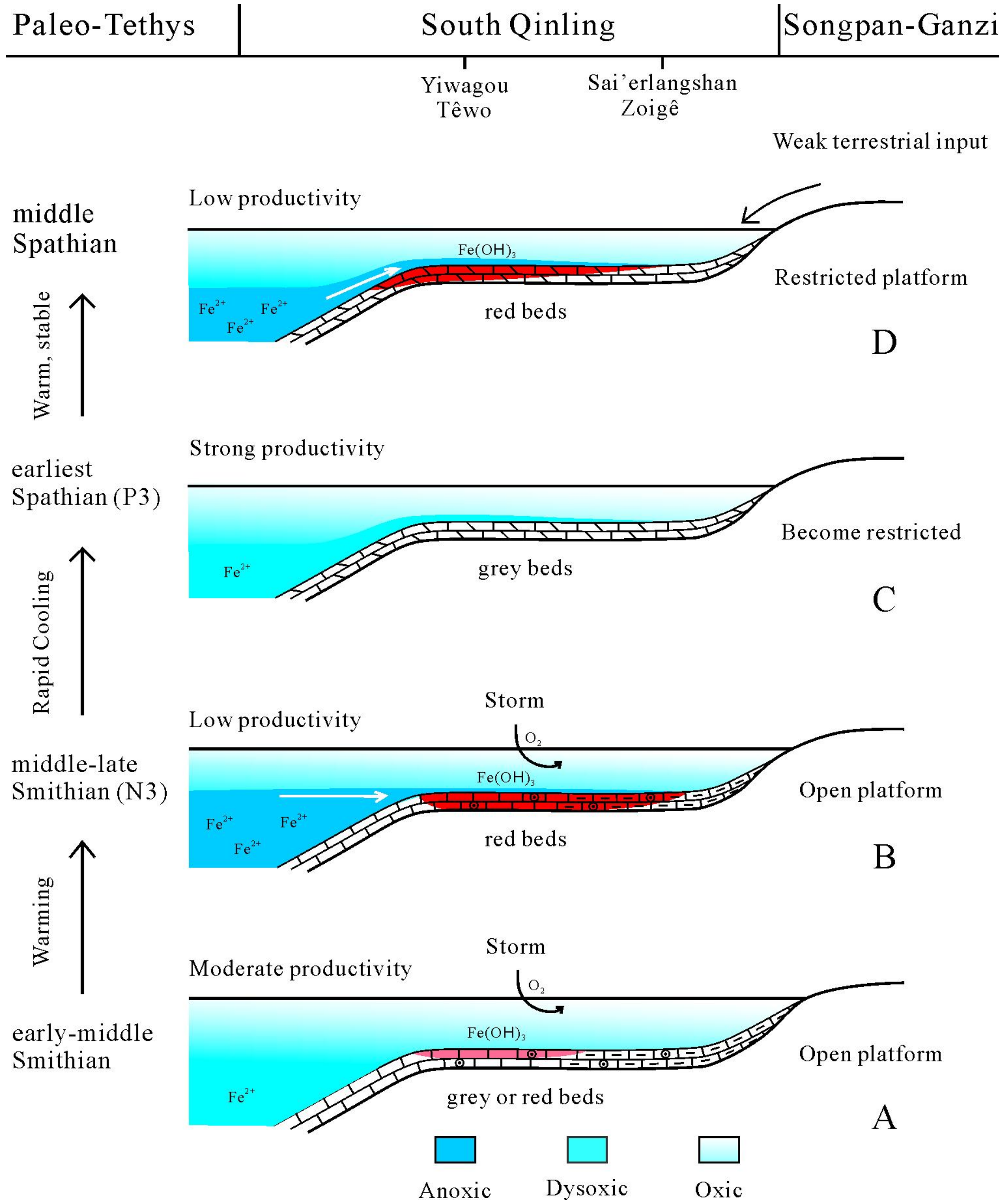
Paleo-Tethys
South Qinling
Songpan-Ganzi
Yiwagou
Têwo
Sai'erlangshan
Zoigê
Weak terrestrial input
middle
Spathian
Low productivity
$Fe(OH)_3$
Restricted platform
Fe^{2+} Fe^{2+} Fe^{2+}
red beds
D
Warm, stable
earliest
Spathian (P3)
Strong productivity
Become restricted
Fe^{2+}
grey beds
C
Rapid Cooling
Storm
Low productivity
O_2
middle-late
Smithian (N3)
$Fe(OH)_3$
Open platform
Fe^{2+} Fe^{2+} Fe^{2+}
red beds
B
Warming
Storm
Moderate productivity
O_2
early-middle
Smithian
$Fe(OH)_3$
Open platform
Fe^{2+}
grey or red beds
A
Anoxic
Dysoxic
Oxic

Figure10

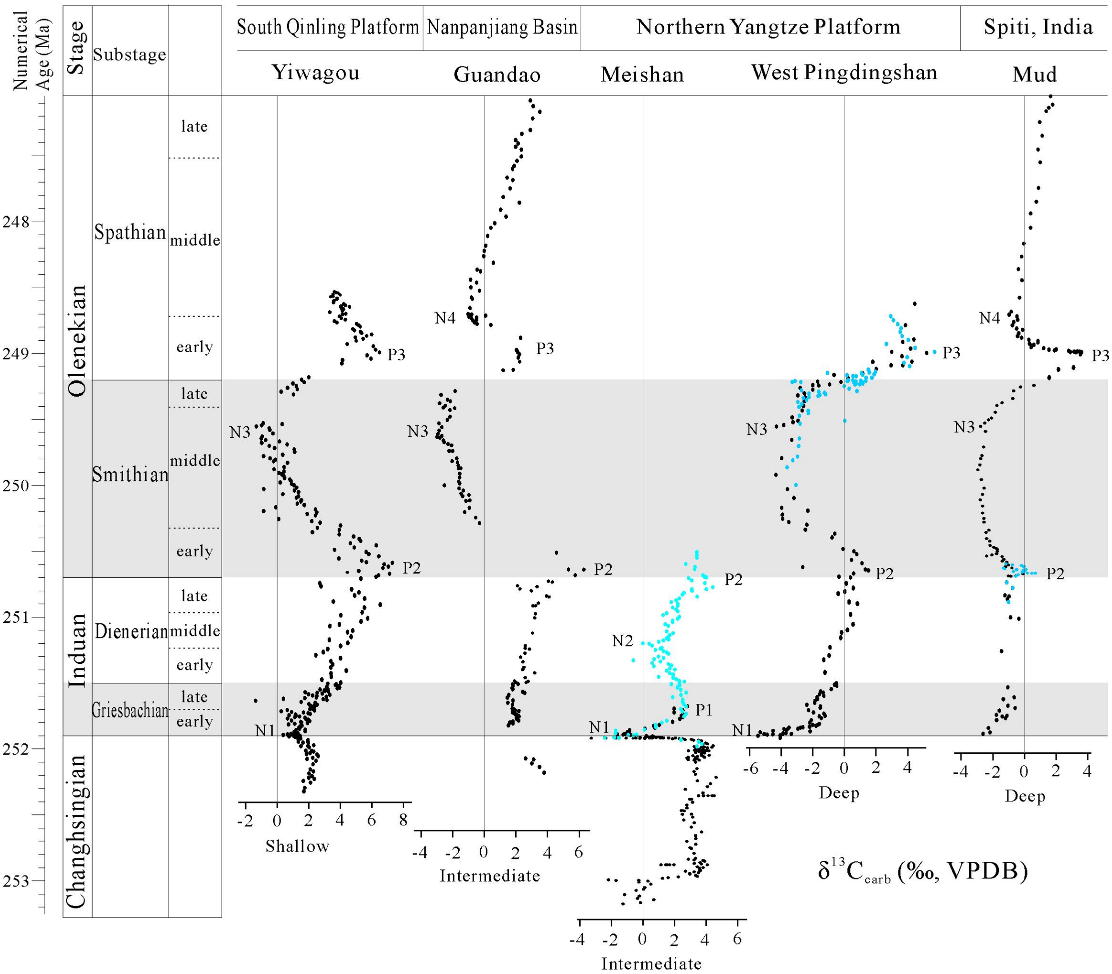

Numerical Age (Ma)
Stage
Substage
South Qinling Platform
Nanpanjiang Basin
Northern Yangtze Platform
Spiti, India
Yiwagou
Guandao
Meishan
West Pingdingshan
Mud
Olenekian
Induan
Changhsingian
Spathian
Smithian
Dienerian
Griesbachian
late
middle
early
248
249
250
251
252
253
N1
N2
N3
N4
P1
P2
P3
Shallow
Intermediate
Deep
δ13Ccarb (‰, VPDB)

Figure11

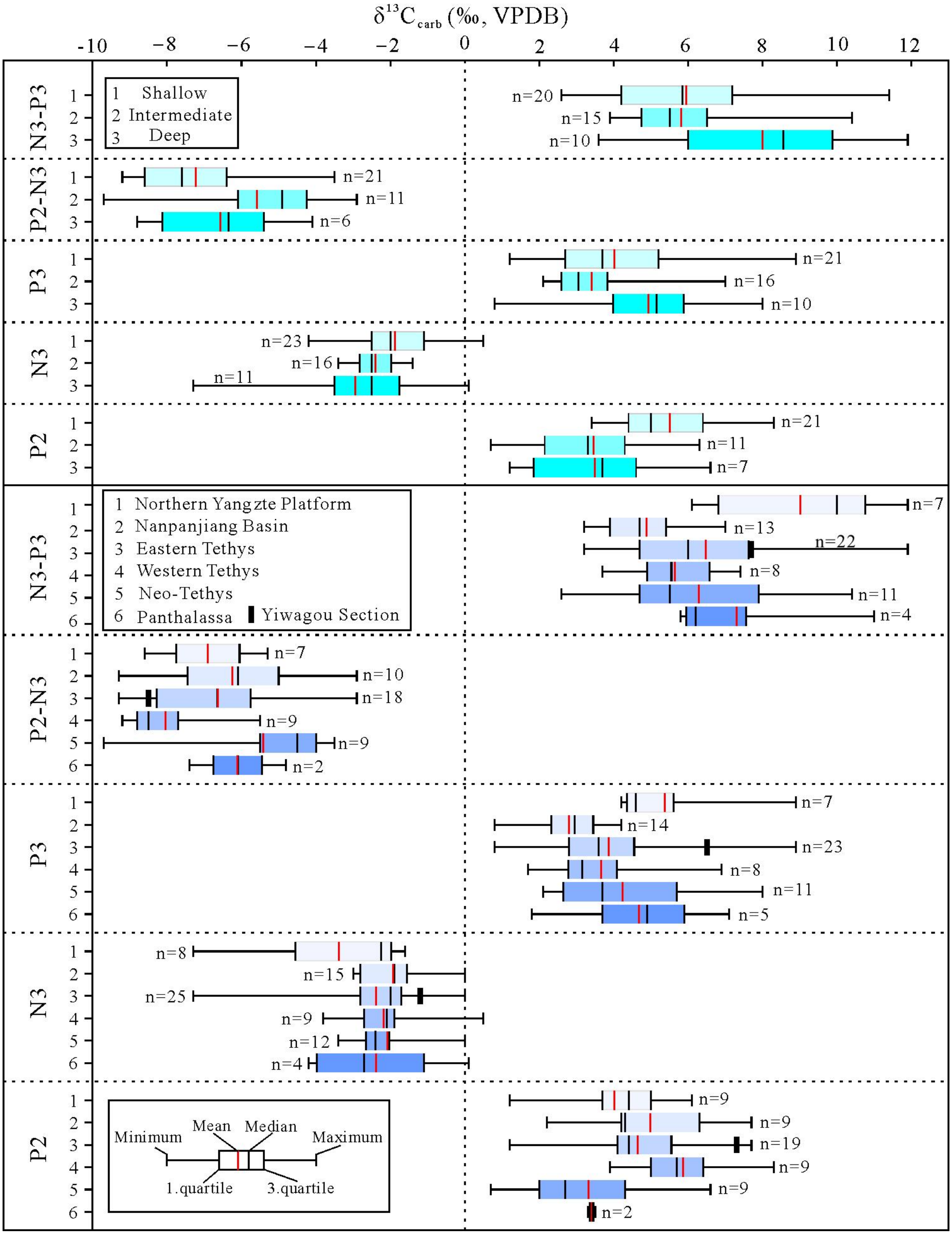

δ13Ccarb (‰, VPDB)
-10
−8
−6
−4
−2
0
2
4
6
8
10
12
N3-P3
P2-N3
P3
N3
P2
1 Shallow
2 Intermediate
3 Deep
1 Northern Yangzte Platform
2 Nanpanjiang Basin
3 Eastern Tethys
4 Western Tethys
5 Neo-Tethys
6 Panthalassa
Yiwagou Section
Minimum
Mean
Median
Maximum
1.quartile
3.quartile
n=20
n=15
n=10
n=21
n=11
n=6
n=21
n=16
n=10
n=23
n=16
n=11
n=21
n=11
n=7
n=7
n=13
n=22
n=8
n=11
n=4
n=7
n=10
n=18
n=9
n=9
n=2
n=7
n=14
n=23
n=8
n=11
n=5
n=8
n=15
n=25
n=9
n=12
n=4
n=9
n=9
n=19
n=9
n=9
n=2

Figure12

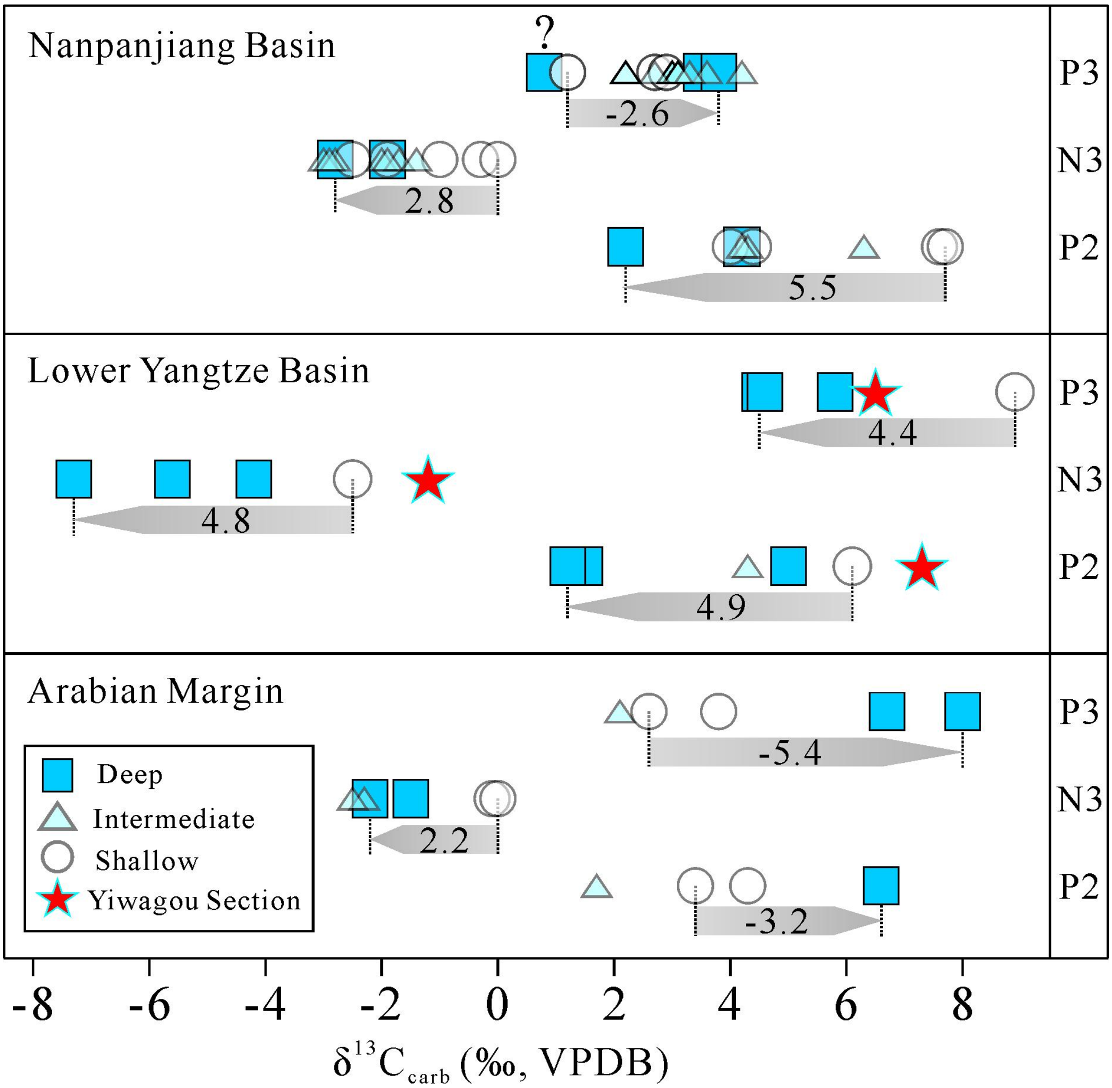

Table1

Association	Microfacies	Lithology	Biogenic content and texture	Sedimentary structure	Depositional setting
1	Mf1	Light grey oolitic grainstone	Abundant concentric ooids, few bioclasts, grain-supported with sparry cement	Thick bedded, ooids and cements are partly dolomitized	Oolitic shoal
2	Mf2	Grey brachiopod-gastropod-peloid packstone/grainstone	Some brachipods, gastropods, algae fragments and peloids, grain-supported	Medium to thick bedded, slightly dolomitized in some parts	Open-marine carbonate platform
	Mf3	Grey or red bivalve-gastropod packstone	Abundant bivalves, gastropods and trace fossils, occasional other bioclasts, fossil fragments have micritic envelopes, common cortoids with bioclasts at the core, grain-supported	Thin to medium bedded	
	Mf4	Grey or red bioclastic wackestone/packstone	Some bivalves, gastropods, foraminifers and trace fossils, occasinal other bioclasts, matrix-supported or grain-supported	Thin to thick bedded	
3	Mf5	Red, pink or grey calcarenites packstone/grainstone, oolitic grainstone	Irregular-shaped, angular intraclasts, small round to subround ooids, bioclasts are mainly conodonts and foraminifers, some bivalve, gastropod and ostracode fragments, occasional sand-sized grains of quartz, grain-supported	Thin to thick bedded, hummocky cross bedding, horizontal bedding,	Storm-dominated inner platform
4	Mf6	Grey or reddish ostracode wackestone/packstone	Some ostracodes, conodonts, peloids and trace fossils, matrix-supported or grain-supported	Thin-bedded micritic limestone, interbedded with medium to thick-bedded limestone, horizontal bedding	Restricted carbonate platform
	Mf7	Light grey crystalline dolomite, dolomicrite, dolomite limestone	Some conodonts, abundant trace fossils, few bioclasts, fine-grained, grey or reddish weathering surface	Thick bedded or massive crystalline dolomite, thin to thick-bedded dolomicrite and dolomite limestone recrystallization filling, pressure-solution structure	
	Mf8	Red or grey peloidal packstone/grainstone	Abundant peloids, foraminifers, conodonts occasional trace fossils, cements are calcite or dolomite crystals	Medium to thick-bedded	